The Fact Of Fractal Tennis: The Universe As A Fractal Computer Defined by the Star=Electron+Atom=Galaxy Quine

Steven E. Elliott

May 2026

Abstract

We propose a new principle of physics—MATHICCS—requiring that every mathematical axiom used in a physical law must correspond to an operation persistently realizable by a physical subsystem. Applying this criterion motivates reality's geometry as a discrete, self-similar, singularity-free structure: the Apollonian Soddy Sphere Packing (ASSP). We conjecture that 3D dynamics on this packing is a *self-computing fractal*: a dynamical computer whose registers are fractal-congruent objects that store angular and linear momentum as cross-scale registers. This fractal quine is proposed as a self-describing, MATHICCS-valid physical theory: it derives the fine-structure constant $\alpha^{-1}_{\mathrm{TFOFT}} = 4\pi^3 + \pi^2 + \pi = 137.036$ from the minimal Presburger computational cost of a Soddy sphere state update, derives the 77-layer star-electron hierarchy from the rank-23 half-boundary mass register, derives the hydrogen binding energy from the Gyro Ball IO equation $E = \alpha^2 m_e c^2/2$, and derives the gravitational constant G from atomic structure by two independent first-principles routes. We present empirical cross-checks involving the 25-arcminute CMB seam, the observed electron/star hierarchy, and the near-match between Karlsson quasar logarithmic periodicity and the derived Info-channel leakage; the Karlsson complement also gives a 77-layer mass-channel spot check inside the same 137–139 register interval. We present one pending falsifiable prediction, $\alpha^{-1}_{\mathrm{Yb}} = 137.035998945 \pm 20\,\mathrm{ppb}$. The framework is presented as a zero-free-parameter ontology whose derived consequences are compared against major tensions in observational physics.

1 Principles: The Motivation for MATHICCS

1.1 The Problem: Operational Constraints on Physical Axioms

Modern physics often employs mathematical structures whose physical realization is left implicit. Consider:

1. **Completed infinities** ($\mathbb{N}$ as a finished object): These are invoked in standard analysis and set theory but cannot be instantiated by any physical clock, apparatus, or experiment.

2. **Limit operations at infinity** ($t \to \infty$, $V \to \infty$): No experiment can directly verify behavior at infinite time or volume.

3. **Infinitesimal quantities and derivative-based formalisms**: Defined by ϵ-δ limits that assume completion of infinite sequences.

4. **Infinitely many degrees of freedom in field theory**: The continuum treats space as uncountably many points, exceeding what can be physically instantiated.

5. **Black-hole singularities**: Divergent density and curvature indicate the model has left its domain of operational validity.

These examples motivate a stricter criterion: a mathematical structure is physically admissible only if its defining operations can be realized by a persistent physical procedure.

1.1.1 General Relativity and the de Sitter Collapse of Operational Clocks

General relativity with $\Lambda > 0$ predicts that expanding FLRW solutions generically approach a de Sitter-like late-time regime consistent with the observed cosmological constant [10]. In de Sitter space the Gibbons–Hawking temperature [37]

$$T_{\mathrm{dS}} = \frac{\hbar c}{2\pi k_B}\sqrt{\frac{\Lambda}{3}}$$

implies that any finite-energy localized configuration radiates thermally. The decay time of a clock of energy E is finite:

$$\tau_{\mathrm{decay}}(E) \sim \frac{3E}{\hbar c \Lambda}.$$

Hence no physical clock survives indefinitely. The set of spacetime regions in which a valid ε-δ measurement apparatus can be maintained shrinks exponentially:

$$\mathcal{V}_{\mathrm{valid}}(t) \propto e^{-t/\tau_{\mathrm{decay}}}, \qquad \lim_{t\to\infty} \mathcal{V}_{\mathrm{valid}}(t) = 0.$$

By MATHICCS M1 any axiom whose realizing apparatus has measure-zero survival probability is MATHICCS-invalid. The Einstein Equivalence Principle therefore has no positive-measure set of initial conditions under which it persists indefinitely.

> **Theorem-like statement.** General relativity is operationally self-limiting under MATHICCS: the cosmological constant required to match observation also destroys the persistent measurement apparatus needed to define the theory's foundational local measurements.

1.1.2 The Role of External Formalism

Independence results in set theory, Gödel incompleteness, and non-constructive continuum assumptions indicate that not every mathematically coherent object is automatically physically realizable [30].

MATHICCS does not invalidate calculus as a computational tool. It distinguishes ontological claims (the continuum *is* reality) from effective approximations (the continuum *describes* reality to bounded error). A computable calculus grounded in ASSP sphere geometry is fully MATHICCS-valid.

1.2 MATHICCS: The Operational Criterion

We propose the following criterion.

> A mathematical axiom is physically valid if and only if there exists a physical subsystem that can instantiate the operation described by the axiom and do so persistently under the evolution laws of the system partially or wholly described by that same axiom.

This criterion is called MATHICCS: *Mathematical Axioms That Have Infinitely Complete Computable Sanity.*

1.2.1 Definition 1: Mathematical Process P

A mathematical process P is any logical operation that appears in an axiom (quantifier, limit, smoothness assumption, cardinality statement, integral, etc.).

1.2.2 Definition 2: Internal Realizer

An internal realizer is a subsystem S composed of clocks, apparatus, and protocols that can instantiate process P to arbitrary finite precision, with precision arbitrarily improvable by expanding S.

1.2.3 Definition 3: Internal Persistence

Process P has internal persistence if there exists a positive-measure set of initial states under which the creation of realizers of P survives indefinitely under the evolution laws dictated by the axioms containing P.

1.2.4 Definition 4: MATHICCS Axiom M1 — Operational Validity

An axiom A containing process P is MATHICCS-valid only if P has internal persistence. This is the Elliott Math Stability Rule (EMSR).

1.2.5 Definition 5: MATHICCS Axiom M2 — Internal Realization

Physical meaning requires demonstration of internal realization. Axioms drawn purely from external set theory, Peano arithmetic, ZFC, large cardinals, or completed ϵ-δ limit processes are not physically admissible unless grounded in a physical subsystem. This is the Internal Realization Requirement (IRR).

1.2.6 Definition 6: MATHICCS Axiom M3 — Ontological Self-Consistency

An ontology O is valid only if all axioms in O satisfy M1 and M2 simultaneously. An ontology that is MATHICCS-valid and matches universal observations to bounded error satisfies the ontological-epistemological equivalence principle (OEEP).

1.3 Why Self-Describing Systems Must Be Gödel-Free

A self-describing physical system is one in which the laws governing the system are themselves encoded as structures within the system. This is the setting in which MATHICCS applies: the realizers of the axioms must persist under the laws those axioms describe.

> **Theorem (Informal):** A MATHICCS-valid self-describing system cannot be governed by an axiomatic system subject to Gödel incompleteness.

Argument. Suppose the system $\mathcal{U}$ is described by an axiomatic system $\mathcal{A}$ that is Gödel-incomplete. Then there exists a true statement S about $\mathcal{U}$'s dynamics that $\mathcal{A}$ cannot prove. But $\mathcal{U}$ must physically realize its own dynamics, including the dynamics described by S. This means that $\mathcal{U}$ performs an operation that its own descriptive language cannot validate. Under M1 any operation in $\mathcal{U}$ must be persistently realizable. A MATHICCS-valid self-describing system is therefore naturally modeled by a complete, consistent, decidable axiomatic framework.

Among known arithmetic systems, Presburger arithmetic (addition and order only, without general multiplication) is complete, consistent, and decidable [19]. These properties make it a natural candidate for the internal arithmetic of a self-describing physical theory.

2 Fractal Law: From MATHICCS to Fractal Geometry

2.1 Why MATHICCS Motivates a Fractal Substrate

2.1.1 Step 1: Replace the Continuum

Standard physics uses $\mathbb{R}$ as the arena for continuous fields, while fractal geometry provides a well-developed language for scale-recursive structures in nature [17, 25]. However, $\mathbb{R}$ is a completed infinity: it contains uncountably many points with no constructive specification. Under M2 this is not an automatically admissible physical assumption. A possible alternative is a recursively refinable discrete structure. At level n there are N_n discrete positions; at level $n+1$ there are $N_{n+1} = kN_n$ for some $k > 1$. This replaces completed infinity with unbounded recursion.

2.1.2 Step 2: Require Persistent Structure

For a physical subsystem to persist, its construction must be stable under evolution. Continuous fields can develop singularities, while discrete self-similar structures avoid such singular points at every scale. This makes self-similar discrete geometry an attractive candidate for a MATHICCS-valid substrate.

2.1.3 Step 3: Fractal Conclusion

Taken together, these considerations suggest that a universe governed by MATHICCS should be discrete at finite resolution, self-similar across scales, stable under its own dynamics, and determined by local tangency relations. The appropriate coarse description of reality is therefore an unbounded fractal with no preferred smallest or largest scale.

3 Evidence for the Fractal ASSP

The principal motivation for the present proposal is the persistence of approximately flat galactic rotation curves, as observed in spiral galaxies including the Milky Way and Andromeda [26, 27], which indicates that orbital speeds remain near-constant over a substantial radial range rather than declining in the Keplerian manner expected from the visible baryonic distribution alone. At the atomic scale, a closely related regularity appears in the quantization of emission frequencies: photons are emitted only at discrete transition frequencies, with photon energy proportional to frequency through $E_{\text{photon}} = h\nu$.

Within the present hypothesis, these two phenomena are treated as scale-related manifestations of a common transfer mechanism. The atom provides the lower-scale electron-to-photon channel, while the galaxy core is conjectured to play the corresponding role for a star-to-macrophoton channel. The observed flat rotation curve would then arise as a lower-scale projection of a more nearly quantized energy-transfer law operating at the higher fractal level.

The empirical case for fractal congruence between atomic and galactic scales—including a $\sim 31\%$ viscous drag signature consistent with a scaled electron-shell contribution to stellar orbital dynamics—is developed in detail in the companion paper [36]. The present paper takes these findings as established and proceeds to the geometric derivation.

3.1 Power Laws and the Apollonian-Soddy Fractal Dimension

3.1.1 Why The ASSP?

A self-similar discrete packing is a natural candidate for a three-dimensional geometry that is simultaneously dense, recursive, and free of singular points, in the spirit of classical fractal geometry and Apollonian packing theory [17, 42, 43, 45]. Sphere packings admit recursive

nesting, avoid edge singularities, and can be specified locally through tangency relations. Among such packings, the Apollonian-Soddy sphere packing is distinguished by its exact recursive geometry and by the determinacy of the Descartes–Soddy curvature relation [40, 42, 43].

More precisely:

- **Perfect self-similarity**: the packing in any region is identical to the packing at any scale, up to constant rescaling.
- **Determinate geometry**: given mutually tangent spheres, the Soddy curvature relation determines subsequent configurations uniquely up to reflection.

3.1.2 Observed Fractal Dimensions

Across a wide range of systems in physics, biology, economics, and geophysics, power-law exponents frequently cluster near values associated here with Apollonian and Soddy-type recursive geometries [17, 45, 42]:

- $\alpha \approx 1.3$: Apollonian gasket dimension ($D_A = 1.305$)
- $\alpha \approx 2.4$: Soddy sphere packing dimension ($D_S = 2.47$)

The clustering is suggestive, though not by itself decisive. Under the present hypothesis, it is consistent with an underlying ASSP-like geometry. Notably, power-law exponents near $D_A \approx 1.3$ recur specifically in systems with radially-defined or rotationally-dominated dynamics (river networks, coastlines, galactic two-point correlation functions), consistent with 2D Apollonian rather than 3D Soddy geometry governing radial scaling at layer boundaries—a distinction made precise in Section 6.2.2.

3.1.3 Universal Power-Law Table

Table 1: Representative power laws across multiple domains, grouped by their proximity to Apollonian or Soddy scaling.

System	**Exponent**	**Fractal D**	**Type**
Astrophysical and Cosmological			
Galaxy two-point correlation function	1.77	≈ 1.2	Apollonian
Cosmic web filament density profile	≈ 2.4	≈ 2.4	Soddy
Interstellar medium density fluctuations	≈ 2.4	≈ 2.4	Soddy
Dark matter halo mass function	1.8–2.0	≈ 2.4	Apollonian/Soddy
Stellar mass function / IMF (Salpeter)	2.35	≈ 2.4	Soddy
Solar wind turbulence spectrum	$5/3 \approx 1.67$	≈ 1.2	Apollonian
Cosmic ray energy spectrum	≈ 2.7	≈ 2.4	Soddy
Asteroid size distribution	≈ 2.5	≈ 2.4	Soddy
Geophysical and Environmental			
Earthquake energy (Gutenberg–Richter)	1.8–2.2	≈ 2.4	Apollonian/Soddy
Forest fire size distribution	1.3–1.9	≈ 1.2	Apollonian
River network branching (Horton's law)	≈ 1.2	≈ 1.2	Apollonian
Coastline fractal dimension (global avg)	≈ 1.2	≈ 1.2	Apollonian
Physical and Chemical			

Continued on next page

System	Exponent	Fractal D	Type
Turbulent energy spectrum (Kolmogorov)	≈ 1.67	≈ 1.2	Apollonian/Soddy
Crack propagation / fracture events	1.2–2.0	≈ 1.2	Apollonian
Magnetic Barkhausen noise	1.3–1.8	≈ 1.2	Apollonian
QCD flux tube (strong force)	≈ 2.4	≈ 2.4	Soddy
Biological			
Neuronal avalanche sizes in cortex	≈ 1.5	≈ 1.2	Apollonian
Neural dendritic arbor dimension	1.2–1.4	≈ 1.2	Apollonian
Lung bronchial branching	≈ 2.4	≈ 2.4	Soddy
Gene regulatory network connectivity	2–3	≈ 2.4	Soddy
Human, Social, and Informational			
Word frequency distributions (Zipf)	1–2	≈ 1.2	Apollonian
City size distributions (Zipf)	1–2	≈ 1.2	Apollonian
Wealth distribution (Pareto tail)	1.5–3	≈ 2.4	Apollonian/Soddy
Internet topology	2–3	≈ 2.4	Soddy

3.1.4 Conclusion: The Fractal Dimension Argument

The recurrence of exponents near the Apollonian and Soddy values is not, by itself, sufficient to establish a unique underlying mechanism. Nonetheless, the pattern is consistent with the ASSP as a candidate geometric substrate. This is the empirical basis for the conjecture stated in Section 4.

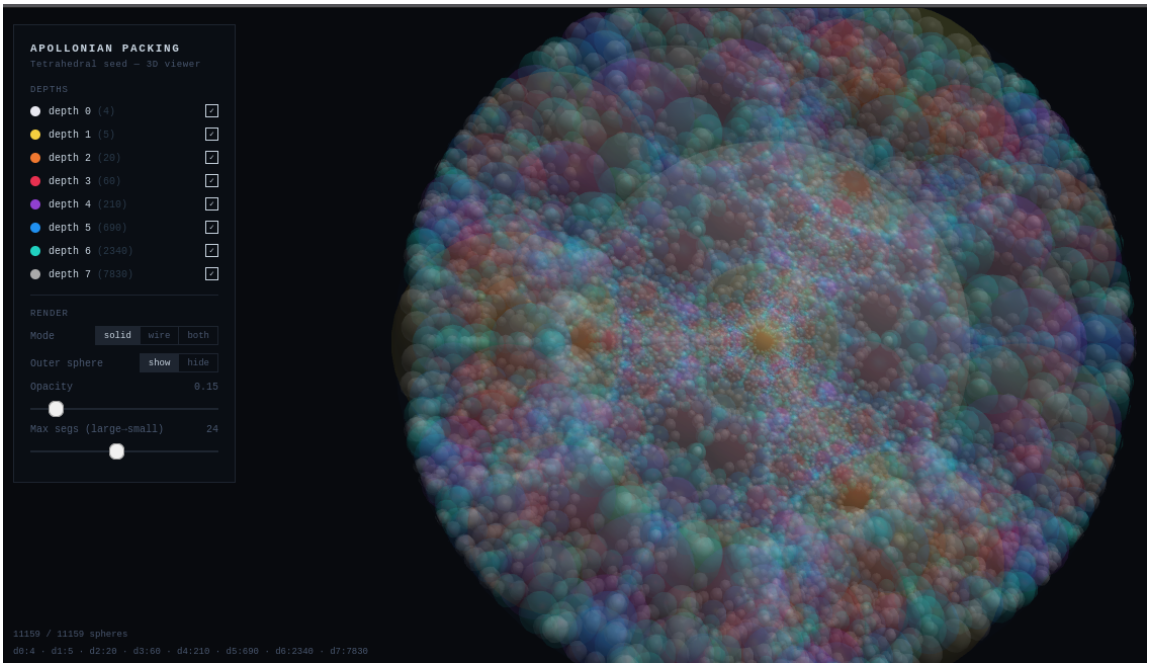

Figure 1: Opaque outline of the tetrahedral seed generating the Soddy cores inside the virtual outer Soddy sphere.

Credit: Generated by Steven E. Elliott.

4 Prior Fractal Physics and the Missing Quine

4.1 A Survey of Fractal Physics Attempts

Fractal geometry has attracted serious attention in physics for decades. Each approach captured part of the truth, but none reached the full self-computing picture. A brief survey:

- **Mandelbrot (1977–1983):** Established that natural systems exhibit fractal geometry; identified power-law scaling and self-similarity as universal features, but offered no dynamical mechanism [17].
- **Garnet Ord / Chaos theory QM (1983):** Showed that random walks on fractal lattices recover structures analogous to relativistic quantum mechanics; insightful but external rules imposed, not self-generated [16]. This result provides important mathematical support for the TFOFT framework.
- **Halton Arp's intrinsic redshift / fractal cosmology (1987–):** Observed that quasar redshift clusters at preferred values and argued against the Big Bang space expansion metric; the logarithmic periodicity is historically associated with Karlsson's preferred-redshift relation [12, 13], but no mechanism for the discretization was provided.
- **Nottale's Scale Relativity (1992–):** Extended relativity to non-differentiable, fractal spacetime and derived quantum-like behavior from fractal geodesics [25]; formally elegant but still grounded in the continuum and limit operations, violating M1. The theory identified the physical law as fractal but did not define congruent physically fractal objects, leaving M3 unaddressed.
- **El Naschie's E-infinity theory (1990s–2000s):** Proposed that spacetime has a fractal Cantorian microstructure with dimension related to the golden ratio; derived $\alpha^{-1} \approx 137$ from Cantorian set theory [54], but relied on completed infinities and non-constructive objects, violating MATHICCS M2.
- **Lestone's string-surface model and α (2007):** Proposed that the fine-structure constant emerges from a heuristic string-like particle-surface model constrained by assumptions inspired by Apollonian circle packing geometry [18]. This yields $\alpha \approx 1/137.04$ without peer review or independent confirmation. It remains the closest geometric precursor to the ASSP but lacks any computational architecture, self-referential quine mechanism, or explicit fractal congruent objects.

4.2 Ord's Fractal Space-Time and the Star-Electron Congruence

Ord (1983) starts from the observation that quantum particle paths are highly irregular and non-differentiable when examined at fine enough scales, and constructs a fractal spacetime analogue of relativistic quantum mechanics [16]. He constructs a continuous but fractal trajectory in spacetime (exemplified by a space-filling Peano-Moore curve with Hausdorff dimension exactly 2 instead of the classical dimension 1). The particle is confined to move on these fractal paths in both space and time. This geometric setup naturally reproduces key quantum features: the uncertainty principle, the de Broglie relation, interference effects, and aspects of relativistic quantum mechanics — all without invoking the full machinery of the Schrödinger equation or path integrals from the start.

When we treat stars as fractal-scale congruents of electrons, and consider electron dynamics to be the low-to-high velocities of ballistic stellar dynamics, which would act like random walks on fractal lattices due to the fractal-like large-scale observed cosmic web structure, this provides direct mathematical support for the cross-scale congruence between stars and electrons in TFOFT.

4.3 What They All Missed: The Fractal Quine

While the theories surveyed above correctly establish that the fundamental dynamics of the universe are fractal at all scales, they stop short of imposing self-referential closure on the fractal law itself through objects within the fractal.

Every prior theory treated the universe as fractal as emergent from dynamics, or fractal law that created no fractal congruent objects. None answered the deeper question: **where do the rules come from, and how does the system enforce them on itself?**

The answer requires three things none of them had:

1. **A MATHICCS-valid axiomatic foundation** (Presburger arithmetic [19]) that is complete, consistent, and decidable—so the system can describe its own operations without Gödel breakage or non-provable, non-physical, non-testable, external processes.

2. **A self-computing architecture.** The dynamical ASSP is conjectured to be not merely a geometric pattern but a dynamical computer. Fractal congruent objects in a fluid-like dynamical system can chaotically evolve into a self-annealing (AI-like) computer system analogous to Turing machines [49, 50]; those fractal congruent objects would then constitute the dynamical computational basis.

3. **The photonic mechanism.** The physical process by which stars fall into galaxy cores, shedding linear momentum as dark matter while transferring angular momentum nonlocally through a different galaxy's polar jets, is conjectured to be the mechanism that replicates the universal fractal computer's operational instructions across layers. Without this process the fractal is merely a pattern; with it, the fractal is a self-running program.

   A fractal that follows external rules is a pattern. A fractal whose rules are encoded, transmitted, and enforced by its own dynamics is a quine. TFOFT is the first attempt at a MATHICCS-valid fractal quine theory of physics.

5 The Fractal Tennis Computer: Ontology and Derived Constants

Status of Claims

This paper combines established mathematical structure with new physical identifications and conjectures. The categories used throughout are:

- **Established background:** standard mathematical and physical results such as Presburger decidability, the Descartes–Soddy relation, Apollonian packing structure, and measured observational quantities.

- **Definitions:** terminology introduced by the present paper, including Star Ball, Core Ball, Gyro Ball, Info Ball, Dust Ball, and the Presburger-ASSP machine.

- **Conjectures:** proposed identifications between the ASSP structure and observed systems, including star/electron congruence, atom/galaxy congruence, dark matter as lower-scale substrate, and force channels as tangency orders.

- **Derived quantities:** quantities obtained internally from the ontology and cost model, including $T_{\text{sphere}} = 4\pi^3 + \pi^2 + \pi$, $\alpha_{\text{TFOFT}}^{-1} = T_{\text{sphere}}$, the rank-23 channel split, the half-boundary mass register, and the resulting 77-layer closure.

Notation distinguishes internally derived quantities (TFOFT) from observed astrophysical/cosmological quantities (obs) and laboratory measurements (meas).

Thus $k_{\text{mass}}^{\text{TFOFT}}$, $T_{\text{mass}}^{\text{TFOFT}}$, and $S_{\text{mass}}^{\text{TFOFT}}$ are ontology-internal quantities, while $\ln(M_\odot/m_e)_{\text{obs}}$, G_{meas}, and α_{meas} are observational or laboratory comparison values.

5.1 The Presburger-ASSP Computational Machine

Standard mathematical formulations of the Standard Model and General Relativity are normally expressed using continuum analysis and arithmetic strong enough to fall within the scope of Gödel-style incompleteness results [30]. These systems cannot prove all true statements about their own arithmetic, creating a fundamental barrier to self-description. In contrast, Presburger arithmetic (addition and order only, without general multiplication) is complete, consistent, and decidable [19]. Multiplication by a *constant* is implemented via repeated addition and is therefore valid; only variable-by-variable multiplication requires indirection. As established in Section 1.3, a MATHICCS-valid self-describing universe is naturally modeled by this arithmetic.

The dynamical Apollonian-Soddy sphere packing (ASSP) operating under Presburger arithmetic is conjectured to constitute a universal computational machine. Unlike the idealized infinite-tape Turing machine, the ASSP machine operates on *finite but recursively expandable tape*, closer in spirit to finite physical computation and self-reproducing automata [49, 51, 50]. At each fractal layer N, the accessible substrate is a locally finite sphere packing with a bounded number of active tangencies. When those tangencies are exhausted, the machine descends to layer $N-1$, adding a finite increment of new capacity. Each expansion step is governed by the Soddy curvature relation, which is a decidable, closed-form computation.

5.1.1 Why the Presburger-ASSP Machine Is Gödel-Free

Gödel incompleteness is a theorem about axiomatic systems that quantify over *completed infinite domains* [30]. It does not apply to finite-tape Turing machines. A machine that operates on a finite tape at each step—even if it can extend that tape by a finite amount after a finite number of steps—never performs unbounded quantification. Every computation it executes is over a finite, explicitly enumerable substrate, and Presburger arithmetic is complete and decidable precisely because it is restricted to such operations [19].

The Presburger-ASSP machine works the same way. The fractal quine derived in Section 5.6 requires approximately 77 recursive log-steps (derived in Section 5.5) to complete one full self-encoding cycle. These 77 steps constitute a *finite* tape execution: the machine reads and writes a finite number of Soddy tangency states, then descends one fractal layer to add more tape. No step requires quantification over a completed infinity. After the 77-step cycle, the machine has reproduced its own initial condition at the next scale layer—its information capacity has effectively doubled through a finite sequence of finite, decidable operations.

> **Axiom P3 (Finite Tape Expansion):** A MATHICCS-valid self-describing machine executes on finite tape at each computational step and possesses a well-defined, decidable mechanism to add finite tape capacity after finite computation. The Presburger-ASSP satisfies this through fractal layer descent governed by the Soddy curvature relation. One complete self-encoding program terminates in approximately 77 finite recursive steps, after which the machine's information capacity has doubled. Gödel incompleteness does not apply: it governs systems that quantify over completed infinite domains, not finite-tape machines with finite expansion rules.

This distinction explains why QFT and GR are not MATHICCS-valid in the sense of M2: both employ completed real-number continua and Peano-arithmetic induction over infinite domains. The ASSP machine never leaves the finite-tape regime. The cost is that it cannot prove

theorems about infinite sets—but a physical computer is not asked to prove such theorems. It is asked to compute its own next state from its current state, which is always a finite-tape operation.

5.2 Lazy Evaluation, Basis Radius Selection, and Presburger Cost Minimization

Presburger arithmetic lacks general variable multiplication; all operations reduce to repeated addition and finite symbol manipulation. In the Presburger-ASSP machine, every symbol, operation, and lookup constitutes a physical computational cost. Arithmetic operations themselves are physical programs executed by the fractal substrate.

The relevant cost is therefore not the Platonic "size" of a number but the total execution cost of the state-update program, in the broad spirit of algorithmic and information-theoretic complexity [48, 46, 47]:

$$C(\mathcal{P}) = C_{\text{lookup}} + C_{\text{op}} + C_{\text{reuse}},$$

where:

- C_{lookup} counts distinct symbol retrievals,
- C_{op} counts repeated-addition execution cost,
- C_{reuse} rewards reuse of already-instantiated basis symbols across multiple channels.

Under MATHICCS there is no ontologically privileged distinction between "numbers" and "programs": the symbols "1", "4", and "π" are themselves persistent physical programs executed by the substrate. Their cost is determined operationally by reuse inside the fractal quine, not by abstract set-theoretic existence.

The complete state-update cost for a single Soddy sphere contains three independent channels:

$$T_{\text{sphere}}(r) = 4\pi r^2 + \pi r + r.$$

The three terms correspond respectively to:

- the surface-area update channel,
- the rotational half-turn phase channel,
- the radial displacement channel.

The critical optimization problem is therefore:

> Choose the basis radius r minimizing the total fractal-quine execution cost by maximizing symbol reuse and minimizing distinct lookup operations during recursive state updates.

Two representative choices illustrate the result:

- **Choice $r = 4$:**

  $$T_{\text{sphere}}(4) = 64\pi + 4\pi + 4 \approx 217.6.$$

  The program must still separately instantiate both the geometric constant π and the basis radius 4. The radius does not absorb the geometric channel structure.

- **Choice $r = \pi$:**

  $$T_{\text{sphere}}(\pi) = 4\pi^3 + \pi^2 + \pi \approx 137.036.$$

  Here the basis radius and the geometric constant become the same persistent symbol. Every channel reuses the identical computational object π, eliminating one entire class of recursive lookup operations throughout the quine.

The reduction is not merely numerical but computational: the fractal quine executes fewer recursive symbol-resolution steps because the sphere radius, rotational arc-length scale, and geometric curvature constant collapse into a single reusable basis program.

> **Axiom P2 (Presburger Minimization Principle):** A MATHICCS-valid self-describing machine selects the basis radius minimizing total recursive execution cost under Presburger operations. The unique radius satisfying maximal geometric-symbol reuse across all three independent Soddy state channels is:
>
> $$\boxed{r = \pi}.$$

This principle is analogous to least action, but applied to computational persistence rather than trajectory optimization: under this ontology the universe evolves toward dynamically reusable code minimizing recursive lookup and execution complexity inside the fractal quine.

5.3 The Three Independent State Channels of a Soddy Sphere

A single Soddy sphere is conjectured to be the minimal self-referential object in the ASSP. Its complete dynamical state requires three orthogonal and independent pieces of information, each corresponding to one Presburger information channel:

- **Surface channel** T_S: Which point on the sphere's surface is currently active? The cost to uniquely specify any point is proportional to the total surface area:

  $$T_S = 4\pi r^2\big|_{r=\pi} = 4\pi^3 \approx 124.025.$$

  This is the Fundamental Area Metric (FAM).

- **Rotational channel** T_R: What is the phase or orientation of the sphere's angular momentum vector? In 3D, rotations are parameterized by points on the unit 3-sphere S^3 with a 2-to-1 covering. The half-turn symmetry means only one hemisphere need be specified, preventing MATHICCS-invalid gimbal lock and multi-valued functions at the poles. The great-circle arc length of one hemisphere at radius $r = \pi$:

  $$T_R = \pi r\big|_{r=\pi} = \pi^2 \approx 9.870.$$

  This is the Fundamental Phase Metric (FPM).

- **Radial channel** T_D: What is the radial distance of the sphere's center from a reference point? The minimum resolvable step is one sphere radius:

  $$T_D = r\big|_{r=\pi} = \pi \approx 3.142.$$

  This is the Fundamental Length Metric (FLM).

5.4 The Fundamental Computational Cost: α^{-1}

The total Presburger cost to fully specify a Soddy sphere's dynamical state is the sum of the three channel costs:

$$T_{\text{sphere}} = T_S + T_R + T_D = 4\pi^3 + \pi^2 + \pi.$$

Numerically:

$$\begin{aligned} 4\pi^3 &= 124.0251067\ldots \\ \pi^2 &= \ 9.8696044\ldots \\ \pi &= \ 3.1415927\ldots \\ \text{Sum} &= 137.0363038\ldots \end{aligned}$$

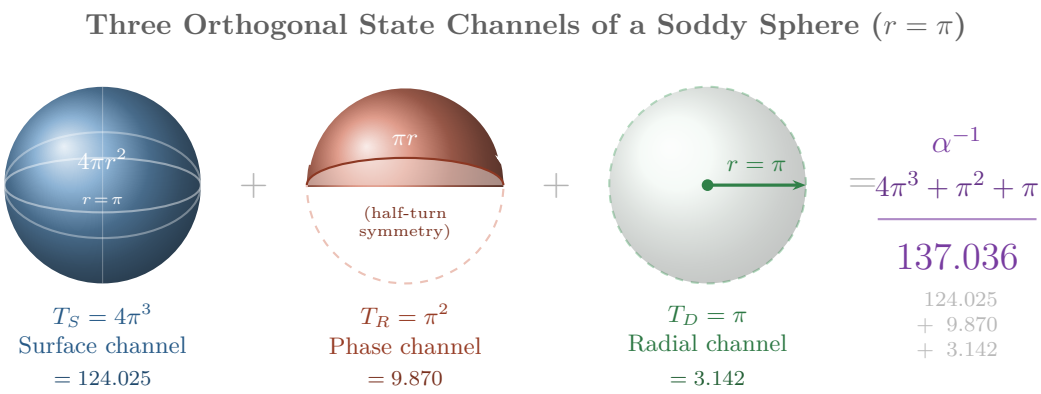

Figure 2: The fine-structure constant α^{-1} as a sum of three orthogonal Presburger information costs for a single Soddy sphere of radius $r = \pi$. **Blue** ($T_S = 4\pi^3$): surface-area channel. **Red** ($T_R = \pi^2$): phase channel (hemisphere only). **Green** ($T_D = \pi$): radial channel. No free parameters; $r = \pi$ is the unique Presburger-minimal radius (Axiom P2).

$$\boxed{T_{\text{sphere}} = 4\pi^3 + \pi^2 + \pi = 137.036}$$

The quantity T_{sphere} is conjectured to be not merely a static information count but the number of effective Presburger log-register updates required to encode one complete Soddy-sphere state inside the fractal quine.

The Presburger-ASSP machine is conjectured to operate asynchronously: no global clock forces neighboring ball-registers to update sequentially. Under this ontology, a complete electromagnetic interaction requires two causally adjacent ball updates to occur in the correct order during post-processing of the full T_{sphere} register stack.

For a fully asynchronous update process, sequential causal alignment between the required two-ball register states occurs with probability inversely proportional to the total quine register depth. The effective sequential-update probability is therefore approximately:

$$P_{\text{seq}} = \frac{1}{T_{\text{sphere}}} = \frac{1}{4\pi^3 + \pi^2 + \pi}.$$

We identify this asynchronous sequential-alignment probability with the electromagnetic coupling strength:

$$\boxed{\alpha = \frac{1}{T_{\text{sphere}}} = \frac{1}{4\pi^3 + \pi^2 + \pi} = \frac{1}{137.036}}$$

Thus, under this ontology, α^{-1} is the effective fractal-quine register depth required to encode one complete Soddy sphere state, while α is the probability that asynchronous Presburger post-processing produces a causally aligned two-ball update during one quine cycle.

Each term is fixed by Presburger minimization and 3D Soddy geometry [19, 40, 42]: $4\pi r^2$ from the surface channel, πr from the hemisphere-restricted rotational phase channel, and r from the minimum radial displacement channel. Setting the Presburger-minimal basis radius $r = \pi$ collapses all three channels onto a single reusable geometric program, minimizing total recursive lookup and execution cost inside the fractal quine. No free parameters are introduced.

Historical attempts to derive or interpret α numerically provide useful context for this claim, although the present derivation is based on a different computational-geometric mechanism [52, 53, 54, 18, 58].

> **Axiom P4 (Elegant Optimized Code):** The operational rules of a self-describing Presburger-ASSP machine minimize information cost subject to MATHICCS constraints. π is preferred over unity as the unit radius because it absorbs all radius

references into a single symbol, reducing the memory footprint of every state update by one lookup. This principle of elegant code is a direct consequence of Axiom P2 and is adopted as a fundamental law of physics under this ontology: the universe computes with minimal memory and computational complexity.

Physical interpretation: α^{-1} measures the total throughput cost (surface, phase, and radial channels combined) for one Presburger tick of a single Soddy sphere. An electromagnetic interaction—a photon coupling to an electron—requires simultaneous state updates of two participating spheres. The coupling constant α is the throughput rate per tick; α^{-1} is the cost.

The value derived here is not obtained by fitting the CODATA recommended least-squares value of α [58]. It is the ontology-internal ASSP value. This distinction is important because the present experimental situation is not perfectly settled: high-precision atom-recoil determinations using cesium and rubidium differ at the several-sigma level. The 2018 cesium measurement gave

$$\alpha_{\mathrm{Cs}}^{-1} = 137.035999046(27),$$

while the 2020 rubidium measurement gave

$$\alpha_{\mathrm{Rb}}^{-1} = 137.035999206(11).$$

The rubidium result was reported as differing by more than five standard deviations from the best cesium-recoil result [56, 57].

Therefore, throughout this paper,

$$\alpha_{\mathrm{ASSP}}^{-1} = 4\pi^3 + \pi^2 + \pi$$

should be read as the predicted ASSP coupling-register depth, not as a least-squares CODATA input.

5.5 The Mass-Channel Split, 77-Layer Self-Encoding, and the He/Fe Garbage Collector

The mass hierarchy is not defined by the observed electron-to-solar mass ratio. It is the self-encoding layer count of a Star Ball mass register consisting of the full single-sphere state plus one half of the rank-23 curvature boundary needed to define that state relationally. The observed electron-to-solar hierarchy is therefore moved to a later cross-check: it tests whether the internal closure lands near the expected astrophysical scale, but it is not an input to the derivation.

5.5.1 The Natural Split from Rank-23 Geometry

The isolated single-ball register is

$$T_{\mathrm{sphere}}^{\mathrm{TFOFT}} = 4\pi^3 + \pi^2 + \pi = 137.0363038.$$

This is the complete Presburger-ASSP state cost of one isolated Soddy sphere. However, a mass hierarchy is not a free-standing isolated sphere. A Star Ball mass register only becomes a physical register when it is relationally defined against a Core Ball boundary. The relevant construction is therefore not the full two-ball transfer register, but the one-register mass channel with a shared relational boundary.

The rank-23 two-ball geometry supplies the raw dual-channel leakage into the Info Ball channel:

$$k_{\mathrm{info}}^{(0),\mathrm{TFOFT}} = 2\left(\frac{23}{27}\right)^2\left(\frac{4}{27}\right).$$

Here 23/27 is the rank-23 curvature fraction relative to the naive 3×3 multiplication count, 4/27 is the addition-only leakage fraction, and the prefactor of 2 counts the two directed boundary legs of the Core–Star transfer. Numerically,

$$k_{\text{info}}^{(0),\text{TFOFT}} = 2\left(\frac{23}{27}\right)^2\left(\frac{4}{27}\right) = 0.2150079.$$

Within the e-clamped two-channel budget, the complementary mass step is therefore

$$k_{\text{mass}}^{\text{TFOFT}} = 2 - k_{\text{info}}^{(0),\text{TFOFT}} = 1.7849921.$$

This value is derived from the rank-23 channel geometry. It is not obtained from $\ln(M_\odot/m_e)_{\text{obs}}$, from Karlsson periodicity, or from any observed mass ratio.

> The raw rank-23 geometry first determines the Info Ball leakage $k_{\text{info}}^{(0),\text{TFOFT}}$. The mass-channel step $k_{\text{mass}}^{\text{TFOFT}}$ is then the complementary e-clamped channel. Observation may later check this value, but it does not define it.

5.5.2 Why 77 Layers: The Half-Boundary Mass Register

The 77-layer count follows from the fact that the Star Ball mass hierarchy is a one-register hierarchy that still requires a relational boundary. It is not the isolated single-ball limit and it is not the full two-ball quine transfer.

The lower limit is the isolated sphere:

$$T_{\text{lower}}^{\text{TFOFT}} = T_{\text{sphere}}^{\text{TFOFT}} = 137.0363038.$$

The full two-ball boundary would add a complete rank-23 curvature boundary:

$$T_{\text{upper}}^{\text{TFOFT}} = T_{\text{sphere}}^{\text{TFOFT}} + \left(\frac{23}{27}\right) = 137.8881556.$$

But the Star Ball mass register receives only half of this boundary, because the boundary is shared relationally between the Star Ball and the Core Ball. Thus the mass register is

$$T_{\text{mass}}^{\text{TFOFT}} = T_{\text{sphere}}^{\text{TFOFT}} + \frac{1}{2}\left(\frac{23}{27}\right).$$

Numerically,

$$T_{\text{mass}}^{\text{TFOFT}} = 137.0363038 + 0.4259259 = 137.4622297.$$

The self-encoding layer count is then the mass-register depth divided by the internally derived mass-channel step:

$$S_{\text{mass}}^{\text{TFOFT}} = \frac{T_{\text{mass}}^{\text{TFOFT}}}{k_{\text{mass}}^{\text{TFOFT}}} = \frac{137.4622297}{1.7849921} = 77.00999 \approx \boxed{77}.$$

This is the central mass-hierarchy derivation. The integer 77 is selected by the half-boundary Star Ball mass register and the rank-23 channel split alone. No observed mass ratio is used to solve for $k_{\text{mass}}^{\text{TFOFT}}$ or $S_{\text{mass}}^{\text{TFOFT}}$.

> A single isolated sphere is a state. A full two-ball register is the quine transfer. The mass hierarchy sits between them: it is the Star Ball's own single-sphere state plus one half of the shared rank-23 curvature boundary. That half-boundary closure pins the self-encoding count at $S_{\text{mass}}^{\text{TFOFT}} \approx 77$.

5.5.3 Interval View of the Mass Register

The half-boundary construction places the mass register between the isolated single-ball limit and the full two-ball boundary limit:

$$T_{\mathrm{sphere}}^{\mathrm{TFOFT}} < T_{\mathrm{mass}}^{\mathrm{TFOFT}} < T_{\mathrm{sphere}}^{\mathrm{TFOFT}} + \frac{23}{27}.$$

Equivalently, in layer units,

$$\frac{T_{\mathrm{sphere}}^{\mathrm{TFOFT}}}{k_{\mathrm{mass}}^{\mathrm{TFOFT}}} = 76.7714,$$

$$\frac{T_{\mathrm{mass}}^{\mathrm{TFOFT}}}{k_{\mathrm{mass}}^{\mathrm{TFOFT}}} = 77.0100,$$

$$\frac{T_{\mathrm{sphere}}^{\mathrm{TFOFT}} + \frac{23}{27}}{k_{\mathrm{mass}}^{\mathrm{TFOFT}}} = 77.2486.$$

Thus 77 is not selected by the lower isolated-sphere limit or by the upper full two-ball transfer. It is selected by the half-boundary mass register.

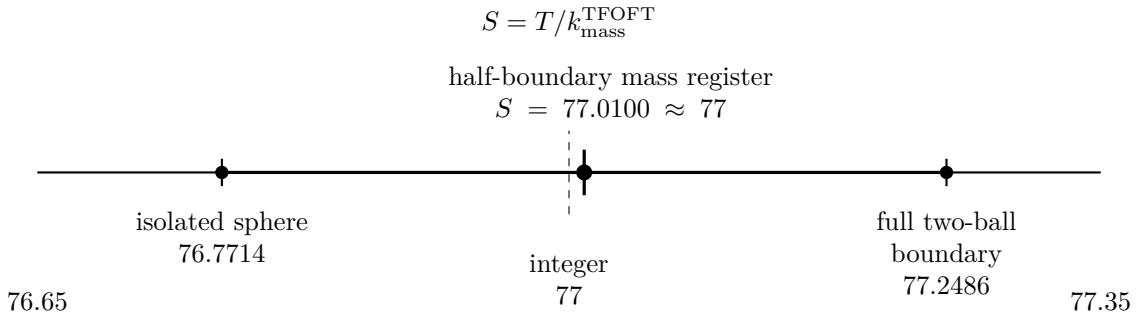

Figure 3: Mass-register interval in layer units. The half-boundary Star Ball mass register gives $S_{\mathrm{mass}}^{\mathrm{TFOFT}} = 77.0100 \approx 77$, between the isolated single-sphere limit and the full two-ball boundary.

5.5.4 Observed Electron-to-Solar Hierarchy

The observed electron-to-solar logarithmic hierarchy is

$$N_{\mathrm{mass}}^{\mathrm{obs}} = \ln(M_\odot/m_e)_{\mathrm{obs}} \approx 138.936.$$

Using the integer closure $S_{\mathrm{mass}}^{\mathrm{TFOFT}} \approx 77$, the corresponding observed effective step is

$$k_{\mathrm{mass}}^{\mathrm{obs}} = \frac{N_{\mathrm{mass}}^{\mathrm{obs}}}{77} \approx 1.80436.$$

The TFOFT mass-channel step is

$$k_{\mathrm{mass}}^{\mathrm{TFOFT}} = 1.7849921,$$

giving

$$\frac{k_{\mathrm{mass}}^{\mathrm{obs}} - k_{\mathrm{mass}}^{\mathrm{TFOFT}}}{k_{\mathrm{mass}}^{\mathrm{TFOFT}}} \approx 1.1\%.$$

This offset is comparable in role to the local virial and density corrections appearing in the G and $\alpha(Z)$ sections.

5.5.5 The 137 − 77 = 60 Residual: He and Fe as Fractal Garbage Collectors

The nearest integer to the single-sphere register depth minus the derived integer mass closure leaves the residual

$$\lfloor \alpha_{\mathrm{TFOFT}}^{-1} \rfloor - S_{\mathrm{mass}}^{\mathrm{TFOFT}} = 137 - 77 = \boxed{60}.$$

We conjecture that this residual encodes the *fractal register garbage collector*: the computational cost of closing the fractal circuit and recycling the momentum debt incurred by mass-channel self-encoding. Persistent computation requires a mechanism to restart fusion processes after a star has exhausted its fuel. The residual Soddy core budget is conjectured to encode the primary fusion endpoints:

- **Helium-4** ($A = 4$): The tetrahedral Soddy-closed shell at four nucleons is conjectured to be the most stable arrangement of simple nucleons in the ASSP. Stability would arise because the external virtual Soddy density exceeds the internal virtual Soddy density, creating a net inward restoring force at every face of the tetrahedron.
- **Iron-56** ($A = 56$): The maximum nucleus for which synthesis still releases energy. Beyond $A = 56$, outer Soddy cores are conjectured to accumulate real curvature faster than inner cores can balance them, and binding energy per nucleon decreases monotonically.

Together,

$$4 + 56 = 60 = \lfloor \alpha_{\mathrm{TFOFT}}^{-1} \rfloor - S_{\mathrm{mass}}^{\mathrm{TFOFT}}.$$

The two dominant nuclear fusion endpoints—helium and iron—are conjectured to be the Soddy-closed garbage-collector states encoded into the arithmetic of fractal self-description: the light and heavy bookends of the 60-unit momentum debt separating the single-sphere register depth from the mass self-encoding layer count.

5.6 The Fractal Quine: Two Balls and the Universal Fundamental Law

The result $T_{\mathrm{sphere}} = 137.036$ is the complete description of a single isolated Soddy sphere. It is a physical constant under this ontology, but not yet a law; a law requires a relation between objects.

When a second sphere is placed in tangency with the first, the system becomes a self-executing program:

1. The first sphere (star ball) encodes angular momentum state into its surface channel $T_S = 4\pi^3$.
2. Tangency with the second sphere (core ball) provides the unique Möbius-invariant coupling: the boundary condition that transfers angular momentum information outward as a linear-momentum carrier.
3. The angular-and-linear momentum wave in the higher fractal layer *is* the info ball—the photon at atomic scale or macrophoton at galactic scale. Its emission transfers the two-ball system's state description non-locally to a third sphere at the same fractal layer.
4. The computational cost of this transfer is paid by injecting dust balls into the lower fractal layer, carrying linear-and-angular momentum as dark-matter production. A secondary cost is the injection of spit balls into the current fractal layer at the non-local ball transfer collision (e.g., AGN jets).

This is conjectured to be the **fractal quine**: the two-ball system writes a copy of its own operational instructions into the info ball it emits.

One ball on top of $T_{\text{sphere}} = 137.036$ is a state. Two balls in tangency is a law. The two-ball configuration is conjectured to be the minimal unit that generates a physical law: the fractal quine instruction set of the Presburger-ASSP.

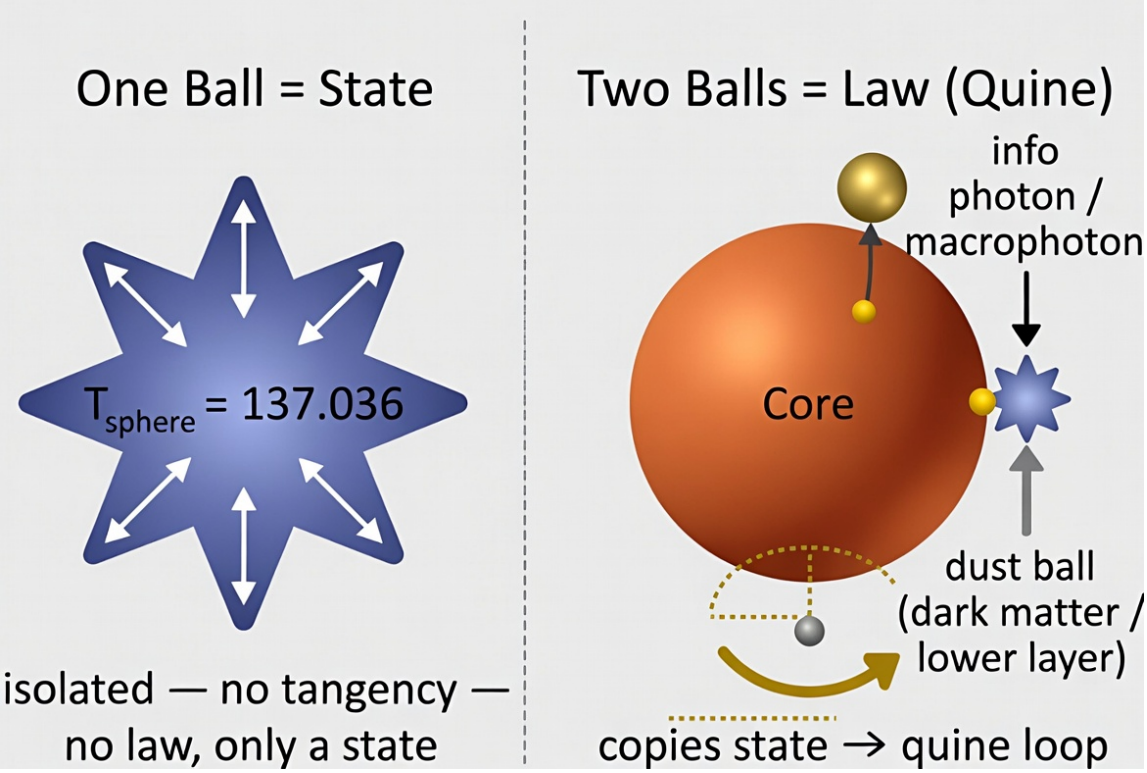

Figure 4: The fractal quine transition. **Left**: a single isolated Soddy sphere carries a complete Presburger state cost $T_{\text{sphere}} = 137.036$ but generates no law. **Right**: a second sphere placed in tangency triggers angular-momentum transfer; an info ball is emitted carrying a copy of the state description. Momentum debt is paid by injecting dust balls into the lower fractal layer (dark matter). The two-ball configuration is conjectured to be the minimal unit that generates a physical law.

5.7 Two-Ball Computational Overhead and the Strassen Geometry

When two balls form a gyro ball, the system promotes a 1D Presburger update into a 3D Euclidean tangency update. The shared angular-momentum state of two tangent spheres requires a 3×3 rotation matrix computation.

Using a Strassen-inspired fast-multiplication analogy, we compare the naive 3×3 multiplication count 27 with the known rank-23 target for general 3×3 matrix multiplication. Strassen's original breakthrough showed that fast matrix multiplication could beat the naive multiplication count for 2×2 matrices, while Laderman later gave a noncommutative algorithm multiplying 3×3 matrices using only 23 multiplications. Modern SAT/search-based work has continued to find and classify rank-23 3×3 schemes, with 23 remaining the lowest multiplication count known for general 3×3 multiplication [21, 1, 2].

- Naïve 3×3: 27 multiplications.
- Strassen-inspired: 23 multiplications, 98 additions.
- Curvature fraction: $23/27 \approx 0.8519$.

- Addition-only fraction: $4/27 \approx 0.1481$.
- Overhead per ball: $\Delta T_{\text{one}} = 23/27$.
- Two-ball overhead: $2 \times 23/27 \approx 1.7037$.
- Dual-channel overhead: $2(23/27)^2(4/27) \approx 0.2150$.
- Total two-ball overhead: $\Delta T_{\text{two-ball}} \approx 1.9187$.

The dual-channel term represents the cost of producing a visible Info Ball transfer through an otherwise dark two-ball Strassen-inspired-overhead state. Both participating balls carry the multiplication-heavy curvature overhead $(23/27)^2$, while the emitted transfer itself exits through the addition-efficient visible channel $4/27$. The prefactor of 2 counts the two directed boundary legs of the Core–Star transfer:

$$\Delta T_{\text{dual}} = 2\left(\frac{23}{27}\right)^2\left(\frac{4}{27}\right) \approx 0.2150.$$

$$\boxed{T_{\text{sphere}} + \Delta T_{\text{two-ball}} = 137.0363 + 1.9187 = 138.9550} \tag{1}$$

The natural logarithm of the electron-to-solar-mass ratio is $\ln(M_\odot/m_e) \approx 138.9357$ [58]. The near-agreement with Eq. (1) is interpreted as a nontrivial structural feature of the Presburger-ASSP architecture under this ontology. Note that $\Delta T_{\text{two-ball}}$ governs the dark matter fraction derived in Section 5.8; it is a separate quantity from the e-clamping layer budget and the two should not be conflated.

5.8 The Dark Matter Fraction from Strassen-inspired Overhead

Using the Strassen-inspired decomposition [21], the addition-only fraction ($4/27 \approx 14.8\%$) represents the computationally *efficient* (luminous) part of each gyro-ball interaction. The multiplication-heavy overhead fraction ($23/27 \approx 85.2\%$) represents the computational cost absorbed into the lower fractal layer, which does not manifest as luminous mass. This is conjectured to be the origin of the dark-matter fraction:

Scale	**Luminous / addition-efficient channel**	**Dark / overhead channel**	**Interpretation**
Atomic	Discrete photonic transition channel	Electron cloud as lower-scale halo analogue	Visible transfer vs. support structure
Galactic	Stars and gas	Dark matter halo	Luminous baryonic layer vs. stabilizing overhead
Cosmic	Baryons and radiation	Dark matter / dark-energy sector	Observable matter vs. curvature-support substrate

Table 2: Fractal congruence of visible and overhead channels. The addition-efficient $4/27$ channel appears as luminous transfer, while the rank-23 overhead channel appears as lower-layer support structure.

This ratio is a prediction of the Presburger-ASSP geometry under the proposed ontology, not a post-hoc fit.

5.9 Atom Base Energy: Deriving the Hydrogen Binding Energy

5.9.1 The Gyro Ball Channel

A gyro ball is one star ball orbiting one core ball—the minimal stable fractal register in the FTC, conjectured to manifest as a hydrogen atom at the atomic scale and as a spiral galaxy at the astrophysical scale.

The electromagnetic channel is conjectured to pass exactly $\alpha = 1/T_{\text{sphere}}$ of the angular momentum per Presburger tick. A complete round-trip (star ball emits, core ball absorbs) requires two channel crossings: one factor of α for emission, one for absorption. The binding energy stabilized by completing a round-trip is:

$$\boxed{E_{\text{atom}} = \frac{\alpha^2 m_{\text{star}} c^2}{2}} \tag{2}$$

5.9.2 Hydrogen: Standard Rydberg Scale Recovered, With the ASSP Giving a 2.22 ppm Offset

For hydrogen ($m_{\text{star}} = m_e$), this reproduces the standard Bohr/Rydberg binding-energy scale [38, 39, 58]:

$$E_H = \frac{\alpha^2 m_e c^2}{2} = \frac{(1/137.036)^2 \times 9.109 \times 10^{-31} \times (2.998 \times 10^8)^2}{2} = 13.606 \text{ eV}.$$

The measured hydrogen ground-state binding energy is approximately 13.606 eV [58]. The agreement is exact to the precision of the input values. The proton mass does not appear because the core absorption rate far exceeds the star emission rate; the star ball alone sets the throughput ceiling.

5.9.3 Heavier Atoms: Local Packing Density Correction

For atomic number $Z > 1$, increased nuclear charge compresses the effective unit radius: $\pi \to \pi(1 + \varepsilon(Z))$, shifting the local coupling:

$$\alpha(Z) = \frac{1}{T_{\text{sphere}}(1 + \varepsilon(Z))^3}, \qquad E_{\text{atom}}(Z) = \frac{\alpha(Z)^2 m_e c^2}{2}.$$

5.10 Kepler's Third Law as the Gyro Ball Clock-Locking Equation

The Gyro Ball interpretation applies not only to the atomic hydrogen binding channel but also to the macroscopic orbital clock of a star around a core. Newton's form of Kepler's third law is [55]

$$T^2 = \frac{4\pi^2}{GM} a^3,$$

where T is the orbital period, a is the semi-major axis, and GM is the gravitational parameter of the core.

Multiplying by the Presburger basis radius $r = \pi$ gives

$$\pi T^2 = 4\pi^3 \frac{a^3}{GM}.$$

Thus Kepler's third law can be written in the ASSP form

$$\boxed{\pi T^2 = 4\pi^3 \mathcal{K}_a} \qquad \text{where} \qquad \mathcal{K}_a = \frac{a^3}{GM}.$$

This is not merely a rescaling of the period. In the FTC interpretation, πT^2 is the orbital clock expressed through the fundamental-radius channel $r = \pi$. The factor $4\pi^3$ is the universal Soddy surface register cost already appearing in the single-sphere state budget,

$$T_S = 4\pi^3.$$

The remaining factor,

$$\mathcal{K}_a = \frac{a^3}{GM},$$

is the local Kepler divider.

The semi-major axis a defines the radius of the virtual Soddy sphere enclosing the Gyro Ball orbit via the tangency chain connecting the Star Ball to the Core Ball boundary. Under this interpretation a^3 is the radial-volume information register of that virtual sphere. The factor GM is the core curvature-throughput rate: the processing strength of the Core Ball boundary. Hence $\mathcal{K}_a$ is the virtual Soddy sphere's information load per unit core throughput.

Equivalently, $\mathcal{K}_a$ is the local clock-divider of the orbital system. A larger virtual Soddy sphere contains more orbital information volume and therefore requires a slower locked output clock. A larger core throughput GM processes that volume faster and shortens the orbital period.

In this form, Kepler's law functions like a phase-locked loop in a physical FPGA. The universal reference is the fundamental-radius channel $r = \pi$. The local oscillator is the visible Gyro Ball orbital period T. The divider is $\mathcal{K}_a = a^3/GM$. A stable orbit is the locked output clock of the system:

$$\text{radius-channel reference} \quad \longrightarrow \quad \text{local Kepler divider} \quad \longrightarrow \quad \text{stable Gyro Ball clock.}$$

Under this ontology, ordinary orbital time is not fundamental in the FTC. It is the relative time generated when the luminous non-Strassen-inspired transfer channel locks to the ASSP radius/surface register. The visible star orbit is the $\sim 4/27$ addition-efficient channel of the two-ball update, while the complementary $\sim 23/27$ Strassen-inspired overhead is paid into lower-layer substrate and appears as dark computational mass rather than luminous Keplerian motion.

The connection to the fine-structure derivation is direct. The full single-sphere register is

$$T_{\text{sphere}} = 4\pi^3 + \pi^2 + \pi,$$

where $4\pi^3$ is the dominant surface channel. Kepler's third law isolates this same leading surface channel and turns it into the observable relative clock of a macroscopic Gyro Ball:

$$\pi T^2 = 4\pi^3 \mathcal{K}_a.$$

Therefore α^{-1} gives the full async single-sphere register depth, while Kepler's law gives the radius-locked relative clock by which visible Gyro Balls execute their luminous orbital updates.

5.11 Rydberg Scaling from Virtual-Core Clock Quantization

The FTC does not quantize free orbits. A Star Ball may evolve continuously under the Gyro Ball Kepler clock until the tangency chain reaches a Core–Star boundary. Quantization enters only at the boundary-transfer event, where the angular-momentum component of the update is copied into an Info Ball channel.

The reason the transfer is quantized is that the Core Ball is not a continuum object. In the FTC ontology, a Core Ball is a virtual boundary-throughput object defined by finite ASSP support around a stable tangency center. That support may be supplied by luminous Star Balls, by Dust Balls and lower-layer substrate, by sub-stellar objects, or by any combination of these

channels. A galaxy core with many visible stars is one realization; a dark-matter-dominated or star-free core is another. Such a "naked" Core Ball is still physically real in the FTC sense if its boundary condition is maintained by lower-layer tangency pressure and substrate flow.

At the galactic scale, the luminous Star Ball population contributes to the center-of-mass and visible Kepler clock of the Core Ball, but it need not supply the whole definition. The remaining support may be carried by Dust Balls, sub-stellar objects, and lower-layer substrate. At the atomic scale, the proton/nuclear core is the corresponding lower-scale Core Ball, while the electron is the Star Ball. The observed atomic clock is therefore a fractal Kepler clock: ordinary atomic time is the lower-scale analogue of the macroscopic Gyro Ball orbital clock.

From the radius-channel Kepler relation derived above,

$$\pi T^2 = 4\pi^3 \mathcal{K}_a,$$

the quantity πT^2 is the orbital clock expressed through the fundamental-radius channel $r = \pi$. It is the internal ASSP clock-cost of the virtual Core–Star system. Photon frequency is the inverse clock output, so boundary-transfer energy is controlled by inverse clock-area:

$$E \propto \frac{1}{T^2}.$$

Let n denote the integer virtual-core clock layer defined by the finite ASSP support of the Core Ball. This support need not be luminous. It may be provided by Star Balls, Dust Balls, sub-stellar registers, lower-layer gas, or any mixture of these components. Thus n is not a Bohr orbit quantum number and not merely a count of visible orbiting bodies. It is the number of completed Kepler-supported or substrate-supported clock layers available to the virtual Core Ball at the boundary-transfer event.

Because the target Info Ball channel must be written into a completed ASSP ball layer, only integer n is allowed. There is no half-layer write target. The n-th virtual-core clock layer satisfies

$$T_n = nT_1.$$

Therefore its inverse clock-area is

$$\frac{1}{T_n^2} = \frac{1}{n^2 T_1^2}.$$

The base Core–Star boundary-transfer energy is the Gyro Ball energy

$$E_{\text{atom}} = \frac{\alpha^2 m_{\text{star}} c^2}{2}.$$

Thus the allowed boundary energies are

$$\boxed{E_n = -\frac{E_{\text{atom}}}{n^2}.}$$

For hydrogen, $m_{\text{star}} = m_e$, so

$$E_{\text{atom}} = 13.606\,\text{eV},$$

and

$$E_n = -\frac{13.606\,\text{eV}}{n^2}.$$

A photon is emitted when the virtual Core Ball relocks from one completed clock layer to another:

$$E_\gamma = E_{\text{atom}} \left(\frac{1}{n_f^2} - \frac{1}{n_i^2} \right).$$

Thus the Rydberg $1/n^2$ law is not imposed by quantized free orbits. It follows from the inverse-square clock-area of a finite virtual Core Ball: the Kepler relation defines ASSP internal time, and discrete ball-layer support quantizes the clock layers at the Core–Star boundary. The emitted Info Ball carries the angular-momentum part of the relocking event, while the complementary linear-momentum cost remains behind in lower-layer substrate.

Virtual-core interpretation. In GR the center of mass is treated as an effective point source for the external metric. In the FTC ontology this point source is not fundamental. It is the here-scale projection of a virtual Core Ball defined by finite ASSP support. For two orbiting bodies, the barycenter is the seed virtual core generated by their mutual Kepler clock. Because gravity couples through multiple fractal layers, the lower-layer substrate does not contain a literal point dipole at the barycenter. Instead it experiences an approximately isotropic response around the virtual core. The standard gravitational field is therefore an emergent effective description of a multi-layer substrate response, not the fundamental object itself.

5.11.1 Finite Lyman and Rydberg Ceilings

The two-ball quine depth provides two distinct spectral ceilings. The direct basis-channel transfer, corresponding to the Lyman series $n_i \to 1$, is limited by the two-ball boundary depth itself:

$$n_{\max}^{\text{Lyman}} \sim T_{\text{two-ball}} \approx 139.$$

This is the maximum direct Core–Star boundary relocking depth into the basis hydrogen register.

At this depth, the last direct Lyman transfer lies only

$$\frac{13.606\,\text{eV}}{139^2} \approx 7.04 \times 10^{-4}\,\text{eV}$$

below the conventional infinite-n Lyman limit. Adjacent terminal Lyman-line spacing near this depth is approximately

$$\Delta E \sim \frac{2(13.606\,\text{eV})}{139^3} \approx 1.0 \times 10^{-5}\,\text{eV}.$$

Therefore ordinary spectroscopy would see the finite basis-channel ceiling as an effective continuum edge unless the experiment resolves sub-meV structure near the Lyman limit and controls broadening effects.

Rydberg-like configurations are different. They are not direct relockings into the basis state but composite excited tangency-chain configurations inside the rotational channel. Since the rotational channel has quadratic subdivision, the effective composite hydrogen address-space ceiling scales as

$$n_{\max}^{\text{H}} \sim (T_{\text{two-ball}})^2 \approx 139^2 \approx 1.93 \times 10^4.$$

This number should be interpreted as the number of principal hydrogen register addresses, not the number of pairwise emitted lines. Spectral lines are relockings between finite register addresses. Therefore the full transition graph can contain many pairwise differences, but it remains finite because the underlying hydrogen register has only finitely many allowed address states.

Thus the FTC does not predict the absence of high-n Rydberg states above $n \approx 139$. It predicts that the direct Lyman basis-channel transfer saturates near $n \approx 139$, while composite Rydberg states can extend to the quadratic rotational-channel ceiling.

5.12 Nuclear Binding Energy: The Soddy Fractal Nucleon Stack

5.12.1 The Soddy Core Concept

In any Apollonian-Soddy sphere packing, a cluster of n mutually tangent equal spheres admits:

- An **inner Soddy sphere** fitting exactly in the central interstice (positive curvature, bending inward).
- A **virtual outer Soddy sphere** circumscribing the cluster (negative curvature, bending outward).

Both are determined uniquely by the Descartes–Soddy relation [40, 42, 43].

5.12.2 Four Nucleons: The Tetrahedral Peak

The minimal 3D Soddy-balanced configuration is four mutually tangent equal spheres arranged in a regular tetrahedron. For this configuration, both inner and outer Soddy cores remain virtual, acting as geometric pressure-balance constraints. The tetrahedral four-nucleon cluster is conjectured to experience maximum restoring force and minimal dislocatability—consistent with ^{4}He having the highest binding energy per nucleon (≈ 7.07 MeV/nucleon) among light nuclei.

5.12.3 Five Nucleons: First Inner Soddy Core Manifests

Adding a fifth nucleon breaks the tetrahedral balance. The inner Soddy core becomes a resolvable packing site while the outer remains virtual. The asymmetric balance is conjectured to reduce binding energy per nucleon—consistent with the absence of stable $A = 5$ nuclei in nature.

5.12.4 The Iron Peak (Conjecture)

Iron (^{56}Fe) is conjectured to sit at the global binding energy maximum (≈ 8.79 MeV/nucleon) because it is the first Soddy iteration at which both inner and outer Soddy cores are simultaneously real and balanced at the same iteration depth. Beyond $A = 56$, outer Soddy cores are conjectured to accumulate real curvature faster than inner cores can balance them.

5.13 Pauli Exclusion from Soddy Uniqueness (Conjecture)

Given any interstice in a locally finite Apollonian-Soddy sphere packing, the corresponding tangent sphere is fixed by the Descartes–Soddy relation, the classical tangency theorem underlying Apollonian packing constructions [40, 42, 43].

We conjecture that this geometric uniqueness is the physical origin of the Pauli exclusion principle: no two star balls can simultaneously occupy the same Soddy interstice. The two allowed spin orientations ($\pm 1/2$) correspond to the two solutions of the Soddy relation with opposite curvature signs (inner vs. outer tangency).

5.14 Antimatter as Möbius-Chirality-Inverted Star Balls (Conjecture)

We conjecture that the positron is a star ball whose electromagnetic handedness has been inverted by a Möbius transformation $r \to R^2/r$. Under Möbius inversion, the surface-normal orientation reverses, flipping the chirality of the angular momentum relative to the orbital plane:

$$\begin{aligned} m_{\text{anti}} &= m_{\text{star}} \quad \text{(mass is a Möbius invariant)} \\ s_{\text{anti}} &= -s_{\text{star}} \\ q_{\text{anti}} &= -q_{\text{star}} \end{aligned}$$

These are the CPT properties of antimatter. The matter–antimatter asymmetry is conjectured to arise because the angular momentum gradient of stellar explosions biases the dominant spin chirality of ejected star balls in the resultant fractal layer, favoring one orientation over the other by a factor of order α.

5.15 Neutrino Flavor Channels as Sub-Stellar Lifecycle Stages

In standard neutrino physics, flavor states ν_e, ν_μ, ν_τ are mixtures of mass eigenstates. Oscillation experiments measure mass-squared differences between the light eigenstates, not three independent classical flavor masses [3]. Therefore the following identification is not a claim that the flavor masses are directly measured as exact values. It is a conjectural FTC interpretation of

the three flavor channels as three lifecycle ceilings, using the direct flavor-channel mass bounds relative to the corresponding charged-lepton Star Ball.

The relevant dimensionless comparison is

$$\frac{m_{\nu_\ell}}{m_\ell} \quad \text{versus} \quad \frac{M_{\text{substellar}}}{M_\odot},$$

where $\ell = e, \mu, \tau$. In the star/electron congruence, the charged lepton is the Star Ball of the corresponding channel, while the neutrino is the passive sub-stellar register beneath that channel.

Using the current direct electron-neutrino effective mass bound from KATRIN,

$$m_{\nu_e} < 0.45\,\text{eV},$$

and the CODATA electron rest energy,

$$m_e c^2 = 0.51099895069\,\text{MeV},$$

one obtains [4, 58]

$$\frac{m_{\nu_e}}{m_e} < 8.8 \times 10^{-7}.$$

This lies in the rocky/terrestrial sub-stellar band:

$$\frac{M_{\text{Mars}}}{M_\odot} \approx 3.2 \times 10^{-7}, \qquad \frac{M_\oplus}{M_\odot} \approx 3.0 \times 10^{-6}.$$

For the muon channel, the direct kinematic bound

$$m_{\nu_\mu} < 0.19\,\text{MeV}$$

and the charged-muon mass

$$m_\mu c^2 = 105.658\,\text{MeV}$$

give [6]

$$\frac{m_{\nu_\mu}}{m_\mu} < \frac{0.19}{105.658} \approx 1.8 \times 10^{-3}.$$

This lies in the gas-giant band:

$$\frac{M_{\text{Jupiter}}}{M_\odot} \approx 9.5 \times 10^{-4}.$$

For the tau channel, the direct kinematic bound from ALEPH,

$$m_{\nu_\tau} < 18.2\,\text{MeV},$$

and the charged-tau mass

$$m_\tau c^2 = 1776.86\,\text{MeV}$$

give [5, 6]

$$\frac{m_{\nu_\tau}}{m_\tau} < \frac{18.2}{1776.86} \approx 1.0 \times 10^{-2}.$$

This lies near the brown-dwarf threshold:

$$\frac{13 M_{\text{Jupiter}}}{M_\odot} \approx 1.24 \times 10^{-2},$$

the approximate deuterium-burning boundary separating giant planets from brown dwarfs. The planetary and sub-stellar mass ratios are taken from standard solar-system mass data [7]. Thus

Channel	Mass ceiling	Sub-stellar regime	Interpretation
Electron flavor	Rocky-planet scale	Terrestrial / metallic bodies	Lowest curvature-storage channel; stable condensed matter regime
Muon flavor	Gas-giant scale	Jovian-class bodies	Intermediate overhead-storage channel with large volatile envelope
Tau flavor	Brown-dwarf scale	Failed-star transition regime	Highest sub-stellar channel before sustained fusion ignition

Table 3: FTC comparison between neutrino flavor-channel mass ceilings and sub-stellar lifecycle stages. The ratios are interpreted as upper channel ceilings rather than exact measured flavor masses. The three channels align with the rocky, gas-giant, and brown-dwarf sub-stellar regimes.

the tau channel is interpreted as the brown-dwarf analogue of the passive sub-stellar register sequence.

Thus the three neutrino channels correspond naturally to the three passive sub-stellar lifecycle stages beneath the main Star Ball regime:

$$\text{rocky} \quad \longrightarrow \quad \text{gas giant} \quad \longrightarrow \quad \text{brown dwarf.}$$

Neutrino oscillation is then conjectured to be the lower-fractal analogue of a sub-stellar object transitioning between passive register regimes under changing local density and pressure.

No fourth light neutrino is expected because no fourth Soddy-stable passive sub-stellar regime is required between the brown-dwarf channel and the active Star Ball regime. This is consistent with the standard three-neutrino mixing picture [3].

5.16 Wave-Particle Duality as Fractal Pilot-Wave Dynamics (Conjecture)

A star ball traversing the region near two adjacent Soddy interstices generates a **Wake Ball**: a fluid-like angular-momentum disturbance propagating through the ASSP fractal substrate, analogous in spirit to hydrodynamic and pilot-wave formulations of quantum mechanics [28, 16, 25]. The interference pattern arises because the Wake Ball explores both interstice paths simultaneously while the star ball follows the gradient of the Wake Ball intensity.

Distinguishing prediction: Standard QM treats slits as boundary conditions defined purely by geometry. TFOFT predicts that the Soddy curvature of the slit material (dependent on atomic number Z and crystal structure) modifies Wake Ball propagation speed:

$$\Delta\phi_{\text{slit}} = \frac{2\pi}{\lambda_{\text{dB}}} \cdot d + \delta\phi(Z, \rho_{\text{slit}})$$

where $\delta\phi(Z, \rho_{\text{slit}})$ is a material-dependent phase shift surviving in the limit of infinitely thin slits. This is in principle falsifiable with high-precision matter-wave interferometry using slits of different materials at identical geometry.

5.17 Pipe Balls: The Fractal Magnetic Field Lines

A **Pipe Ball** is an elongated, quasi-one-dimensional chain of Soddy tangencies in the lower fractal layer, oriented along the gradient of the here-scale angular momentum field. It acts as the fractal-scale analogue of a magnetic field line: a low-density highway of lower-scale hydrogen substrate.

In standard magnetohydrodynamics, magnetic field lines are mathematical constructs. In TFOFT, galactic-scale magnetic field lines are conjectured to be physical Pipe Balls tracing the angular momentum gradient of the local ASSP. The inter-galactic filaments of the cosmic web are their here-scale manifestation at the wish-scale.

5.18 The Ball Ontology: Fundamental Objects of the FTC

5.18.1 Cross-Scale Notation

We define three scale prefixes: **atom** = atomic scale; **here** = galactic/stellar scale; **wish** = the scale above the galactic, where our galaxy plays the role that an atom plays at our scale.

5.19 Soddy Dynamics, Forces, and the Emergence of Gravity

5.19.1 The Soddy Curvature Relation

The fundamental equation governing the sphere packing is the Soddy relation [40, 42, 43]:

$$\left(\sum_{i=1}^{4} k_i\right)^2 = 2\sum_{i=1}^{4} k_i^2.$$

Given four mutually tangent spheres with curvatures $k_i = 1/r_i$, the curvature of a fifth tangent sphere is uniquely determined:

$$k_5 = \sum_{i=1}^{4} k_i \pm 2\sqrt{\sum_{i<j} k_i k_j}.$$

5.19.2 Möbius Invariance and Boundary Crossing

The Soddy relation is invariant under Möbius transformations. At the fractal boundary, an infalling star ball carries angular momentum $\mathbf{L} = m\mathbf{r} \times \mathbf{v}$. Möbius inversion preserves $\mathbf{L}$:

$$\mathbf{L}_{\text{after}} = \mathbf{L}_{\text{before}}.$$

The ball emerges into the higher scale as an info ball with energy scaled by λ^2 (where $\lambda \approx 10^{31}$ is the inter-layer scale factor). Linear momentum, which depends on absolute velocity, does not survive the crossing. Angular momentum, which is frame-independent and scale-invariant by definition, is the conserved quantity carrying information across fractal layers.

5.19.3 Coupling Strength Hierarchy: Four Forces from Four Tangency Orders

The Soddy relation involves exactly 4 mutually tangent spheres. These interact at different tangency orders, producing four distinct coupling strengths:

1. **1st-order tangency** (one sphere touches one other): $\alpha_{\text{EM}} = 1/137$ (Electromagnetic)
2. **2nd-order tangency** (one sphere touches two others): $\alpha_W = \alpha_{\text{EM}}/4$ (Weak nuclear)
3. **3rd-order tangency** (one sphere touches three others): $\alpha_S \sim \alpha_{\text{EM}}/16$ (Strong nuclear)
4. **0th-order (global metric)**: Gravity (averaged over the full packing)

We conjecture that the four fundamental forces correspond to four distinct interaction orders of the Soddy tangency geometry. The Standard Model gauge group $U(1) \times SU(2) \times SU(3)$ is conjectured to arise from the tangency order symmetries: $U(1)$ from 1st-order single tangency; $SU(2)$ from 2nd-order double tangency with its quaternionic double-cover structure; $SU(3)$ from the 3-coloring of a triple-tangency configuration. This is a conjecture; formalizing it is left to future work.

5.19.4 Laurent Expansion of the Möbius Map

The Möbius map near a tangency point at $r = r_0$ gives an effective gravitational acceleration expanded around the Soddy core radius $r_s = 2GM/c^2$:

$$a_{\text{grav}}(r) = \frac{2v^2}{r} - \frac{4v^2 r_s}{r^2} + \frac{6v^2 r_s^2}{r^3} - \frac{8v^2 r_s^3}{r^4} + \mathcal{O}(r_s^4/r^5) \tag{3}$$

In any given physical interaction, G, M, and m are constants; only r varies. The $1/r^2$ dependence arises from the first-order term above—a rational function of r with constant coefficients, entirely within Presburger arithmetic (constant multiplication = repeated addition).

The zeroth-order term is consistent with flat galactic rotation curves directly from the Möbius geometry, without requiring additional dark matter at large radius. General Relativity emerges as the first-order approximation to Möbius-ASSP geometry under this ontology, valid when $r \gg r_s$.

5.19.5 Gravity Emerges from Geometry

Gravity is conjectured not to be a fundamental force in the TFOFT picture, but the effective geometric consequence of Soddy packing boundary curvature at the fractal layer interface, operating under conservation of angular momentum across the boundary. The gravitational constant G is therefore conjectured not to be an independent fundamental constant but to emerge from the geometry of the ASSP and the Presburger computational constraints—consistent with its independent derivation in Section 6 from the hierarchy depths and fractal dimension.

5.20 The Non-Darkness of Dark Matter: Fractal Electron Manufacture

The term "dark matter" is a historical label. In TFOFT, dark matter is conjectured to be **lower-scale hydrogen gas**—the cold, diffuse hydrogen fuel of the star balls we identify as electrons at the here-scale.

Close to a gravitational well, this substrate becomes locally dense enough to undergo its own fractal-scale stellar generation. Lower-scale hydrogen gas at sufficient pressure ignites lower-scale fusion, producing here-scale electrons. To a here-scale observer, its energy output is conjectured to manifest as anomalous heating in dense compact objects, the Fermi bubbles (Section 6.6.3), and the warm-hot intergalactic medium.

> Dark matter halos manufacture electrons.
> Electron clouds manufacture lower-scale electrons.
> The fractal substrate manufactures itself.

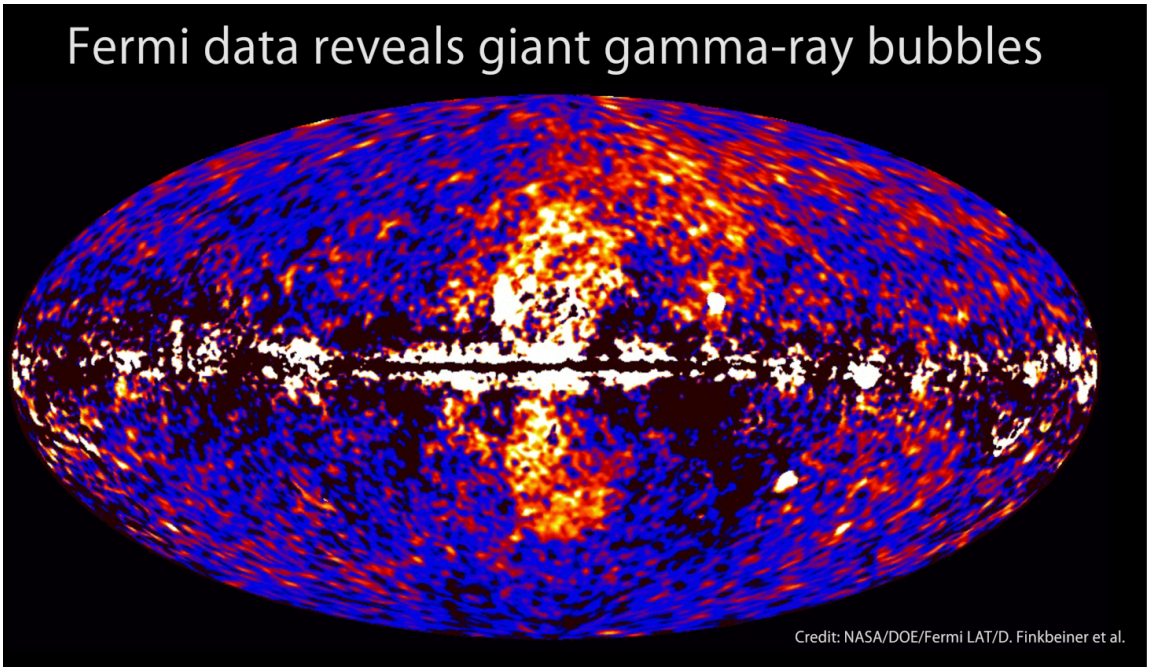

Figure 5: Fermi bubbles observed by the Fermi Large Area Telescope. The two giant lobes extend $\approx$ 50 kly above and below the galactic plane. In TFOFT these are interpreted as the visible signature of lower-fractal-layer hydrogen fusion inside the dark-matter halo (the scaled "$3d_{z^2}$" orbital shell of the galactic fractal hydrogen atom). The predicted bubble height ($\frac{23}{27}R_{\text{halo}} = 49.8$ kly) matches the observed $\approx$ 50 kly to 0.4%. The observed lobe offset from the galactic z-axis ($\approx$ 55–60°) is consistent with the $3d_{z^2}$ nodal cone half-angle $\arccos(1/\sqrt{3}) \approx 54.7°$—a parameter-free geometric prediction of the ASSP orbital shell model.

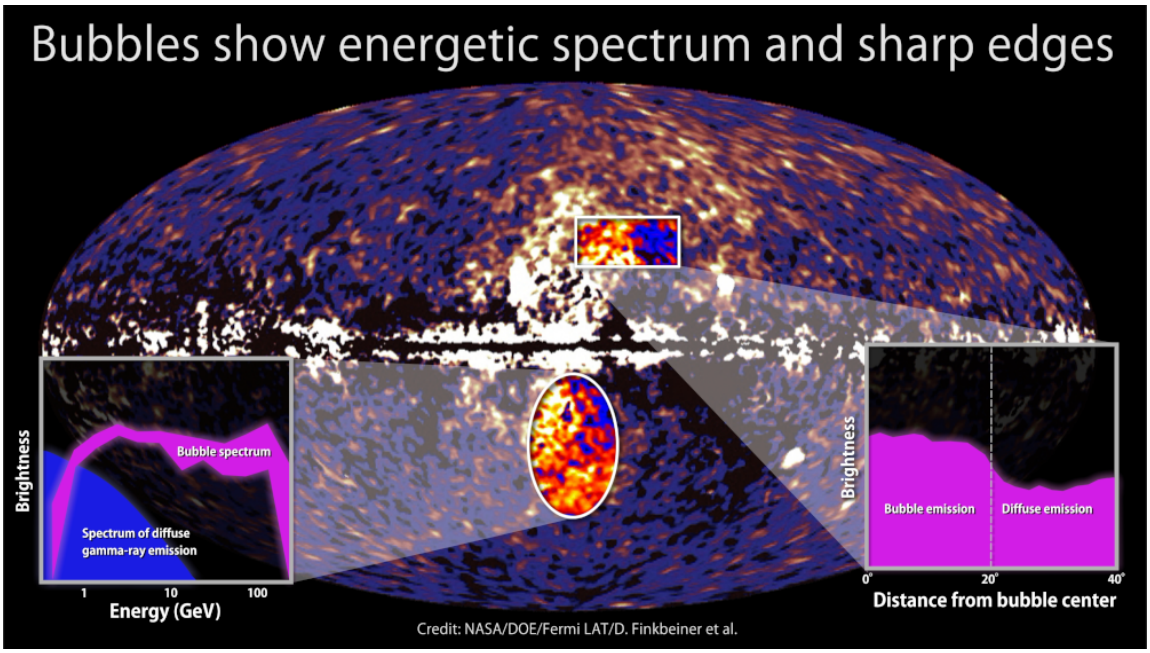

Figure 6: Same Fermi bubbles with insets showing the hard power-law spectrum inside the bubbles versus the diffuse galactic emission, and the extremely sharp edge consistent with a Soddy-sphere boundary in the fractal dark-matter halo.

Credit (both panels): NASA/DOE/Fermi LAT/D. Finkbeiner et al. Source: NASA SVS #10688. Original discovery and subsequent morphology studies: Su, Slatyer & Finkbeiner; Dobler et al.; Ackermann et al. [31, 32, 33].

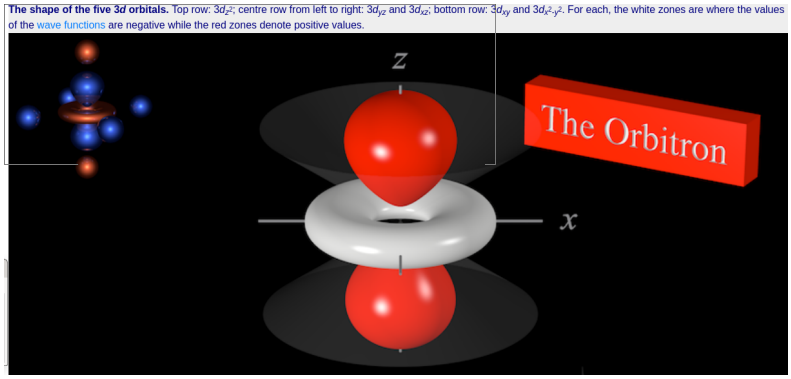

Figure 7: The hydrogen $3d_{z^2}$ orbital (probability density isosurface). The nodal cone half-angle is $\arccos(1/\sqrt{3}) \approx 54.7°$ from the z-axis—fixed by quantum mechanics with no free parameters. The observed Fermi bubble offset of ≈ 55–$60°$ from the Milky Way's rotation axis matches this value, supporting the identification of the dark-matter halo as the galactic-scale analogue of the $3d_{z^2}$ orbital shell.

Credit: Chemistry LibreTexts / Orbitron (M. Winter, Univ. Sheffield). Public domain for academic use.

At every fractal scale N, the orbital shell of scale-N objects around scale-N cores is conjectured to be the dark matter halo of scale N. At sufficient density, this shell spontaneously generates scale-$(N-1)$ objects—a subset of the fractal quine instruction set executing itself at every scale simultaneously.

6 Observational Evidence, Derived Constants, and Predictions

6.1 Quasars as Candidate Info Balls and the Karlsson Logarithmic Periodicity

6.1.1 Redshift as Angular-Momentum Loss

In the TFOFT framework, cosmological redshift is conjectured to be not the expansion of a space metric, but the accumulation of angular-momentum loss as photons traverse fractal layer boundaries. At each boundary crossing, angular momentum is partially transferred to lower-fractal-layer hydrogen gas. Since angular momentum sets the internal clock tick rate, its loss produces a frequency decrease:

$$p = hf/c \qquad \Longrightarrow \qquad \text{if } p \text{ decreases, then } f \text{ decreases.}$$

For a Brownian path through the fractal substrate,

$$z_{\text{Brownian}} \propto \ln(r_{\text{linear}}) \qquad \Longrightarrow \qquad r_{\text{linear}} \approx \exp(z/\text{constant}).$$

The fractal equivalence and the statistical nature of the two-component redshift together imply that the observable universe is, in TFOFT, a vast sphere of hydrogen gas isotropically emitted by a single parent macro-star (the wish-scale analogue of a star). All subsequent structure—galaxies, quasars, the CMB—arises from the internal dynamics of that ejected hydrogen plasma as it self-organizes into the fractal quine.

6.1.2 Karlsson Periodicity as an Info-Channel Check

Karlsson's reported quasar spacing is

$$\Delta \log_{10}(1+z)_{\text{obs}} = 0.089,$$

or

$$k^{\mathrm{obs}}_{\mathrm{Karlsson}} = 0.089 \ln 10 = 0.2049301.$$

The TFOFT Info-channel leakage is

$$k^{(0),\mathrm{TFOFT}}_{\mathrm{info}} = 2\left(\frac{23}{27}\right)^2\left(\frac{4}{27}\right) = 0.2150079.$$

Thus

$$k^{\mathrm{obs}}_{\mathrm{Karlsson}} = 0.2049301, \qquad k^{(0),\mathrm{TFOFT}}_{\mathrm{info}} = 0.2150079,$$

with fractional separation

$$\frac{k^{(0),\mathrm{TFOFT}}_{\mathrm{info}} - k^{\mathrm{obs}}_{\mathrm{Karlsson}}}{k^{(0),\mathrm{TFOFT}}_{\mathrm{info}}} \approx 4.7\%.$$

This near-match motivates the identification of quasars as candidate macroscopic Info Ball events: high-angular-momentum macrophoton-like transfer events associated with parent macro-star/Core Ball coupling.

6.1.3 The Karlsson Complement and the 137–139 Register Window

The e-clamped complement of the observed Karlsson spacing is

$$k^{\mathrm{obs}}_{\mathrm{mass|Karlsson}} = 2 - k^{\mathrm{obs}}_{\mathrm{Karlsson}} = 1.7950699.$$

Across 77 layers,

$$77k^{\mathrm{obs}}_{\mathrm{mass|Karlsson}} = 138.2204.$$

The CODATA/solar electron-star hierarchy is

$$N^{\mathrm{obs}}_{\mathrm{mass}} = \ln(M_\odot/m_e)_{\mathrm{obs}} \approx 138.93575.$$

The resulting interval is

$$137.0363 < 138.2204 < 138.93575 < 139.$$

The Karlsson-complement value is below the observed electron-star hierarchy by

$$138.93575 - 138.2204 = 0.7154,$$

or about 0.5%.

The full TFOFT two-ball transfer register is

$$T^{\mathrm{TFOFT}}_{\text{two-ball}} = T^{\mathrm{TFOFT}}_{\mathrm{sphere}} + \Delta T^{\mathrm{TFOFT}}_{\text{two-ball}} = 137.0363 + 1.9187 = 138.9550.$$

Its separation from the observed electron-star hierarchy is

$$138.9550 - 138.93575 = 0.0193,$$

or 0.014%.

Thus

$$\begin{aligned} T^{\mathrm{TFOFT}}_{\mathrm{sphere}} &= 137.0363, \\ 77k^{\mathrm{obs}}_{\mathrm{mass|Karlsson}} &= 138.2204, \\ N^{\mathrm{obs}}_{\mathrm{mass}} &= 138.93575, \\ T^{\mathrm{TFOFT}}_{\text{two-ball}} &= 138.9550. \end{aligned}$$

6.2 Logarithmic Scale Ratios: Mass, Radius, and Time Hierarchies

6.2.1 Mass Hierarchy: Electron to Star

The observed electron-to-solar mass hierarchy is retained here as an empirical comparison value:

$$N_{\text{mass}}^{\text{obs}} = \ln\left(\frac{M_\odot}{m_e}\right)_{\text{obs}} \approx 138.93575.$$

The TFOFT-derived mass closure $S_{\text{mass}}^{\text{TFOFT}} \approx 77$ is derived earlier from the rank-23 half-boundary mass register, not from this observed ratio. The comparison is that the observed electron-star hierarchy lies near the full two-ball transfer register:

$$N_{\text{mass}}^{\text{obs}} = 138.93575 \approx T_{\text{two-ball}}^{\text{TFOFT}} = 138.9550.$$

This agreement is treated as an observational cross-check of the mass-registerarchitecture, not as an input to the derivation.

6.2.2 Radius Hierarchy: Why the Boundary Is Apollonian, Not Soddy

The 3D bulk dynamics of the ASSP operate under the full Soddy sphere packing, whose Hausdorff dimension is $D_S = 2.474$ and whose computational cost per sphere is $T_{\text{sphere}} = 137.036$. However, the *inter-layer boundary* where the radius hierarchy is measured is not a 3D bulk interaction—it is a 2D one, and the physical reason is rooted in the dynamics of the gyro balls themselves.

The here-scale universe is an ensemble of gyro balls (spiral galaxies) embedded in a medium of lower-scale hydrogen gas (dark matter). Each gyro ball is a rotating disk: its angular momentum is stored and transferred primarily within the disk plane. When two gyro balls interact gravitationally—whether in a near-encounter or a slow cosmological drift—the dominant interaction closely resembles specular elastic collision rather than direct coupling. This is a known statistical result: in a gas of particles with long-range $1/r^2$ interactions and equal masses, most encounters are hyperbolic or parabolic fly-throughs. In the center-of-mass frame, a gravitational deflection by angle θ is mathematically equivalent to a specular elastic collision with the same deflection angle [22]. For equal-mass objects, the two descriptions are physically indistinguishable. This is the microscopic basis of violent relaxation and the reason virialized galaxy clusters obey Maxwell–Boltzmann-like velocity distributions.

The dark matter halo (Dust Ball layer) surrounding each gyro ball acts as the inertial medium: it absorbs and redistributes linear momentum between encounters, providing an effective isotropic pressure that prevents gravitational collapse at the layer boundary. This is the here-scale analogue of Brownian gas pressure—the "anti-gravity" or normal force that caps the full 3D Soddy dynamics at a 2D boundary.

The key consequence is that because the dominant inter-gyro-ball interaction is specular billiard-like, and because rotation selects the disk plane as the preferred 2D surface, the boundary dynamics at each fractal layer interface are governed by **2D Apollonian circle packing** rather than 3D Soddy sphere packing. In 2D, mutually tangent circles with specular reflection at contact points generate Apollonian packings; this is the geometric content of iterated circle inversions, which are the 2D analogue of specular reflection. The Apollonian circle packing has Hausdorff dimension $D_A = 1.305687$ and is governed by the quadratic fixed-point scaling relation [42, 43, 45]:

$$k^2 + k - 1 = 0 \qquad \Rightarrow \qquad k = \frac{\sqrt{5}-1}{2} = \frac{1}{\varphi},$$

where φ is the golden ratio. This is the natural fixed-point scaling of 2D specular tangency chains.

The fractal dimension evidence reviewed earlier supports this assignment: power-law exponents near $D_A \approx 1.3$ recur specifically in systems with rotationally dominated or radially defined dynamics, while the 3D Soddy exponent $D_S \approx 2.4$ governs bulk volumetric systems.

The effective ideal fractal depth of the radius hierarchy is therefore the Apollonian boundary projection of the Presburger fine-structure depth:

$$\alpha_{\mathrm{ASSP}}^{-1} = 4\pi^3 + \pi^2 + \pi = 137.0363038\ldots$$

and

$$\boxed{N_{\mathrm{radius}} = \frac{\alpha_{\mathrm{ASSP}}^{-1}}{\varphi} = \frac{137.0363038}{1.6180339887} = 84.6931.}$$

This is not a fit parameter. It is the direct consequence of two independent results: the Presburger-derived fine-structure depth $\alpha_{\mathrm{ASSP}}^{-1} = 137.0363038$ (Section 5.4) and the Apollonian boundary condition $k = 1/\varphi$ imposed by the specular billiard dynamics of rotating gyro balls at the layer interface. The 3D-to-2D projection—from full Soddy bulk to Apollonian boundary—is the geometric reason that the radius hierarchy uses

$$N_{\mathrm{radius}} = \alpha_{\mathrm{ASSP}}^{-1}/\varphi$$

rather than $\alpha_{\mathrm{ASSP}}^{-1}$ itself.

The convergence of the radius hierarchy to the Apollonian-projected depth $N_{\mathrm{radius}} = 84.6931$ is presented as structural evidence that the star-packing geometry inside galaxies follows the same boundary-projection rules as the fractal radius hierarchy itself. The exact golden-ratio projection gives the homogeneous ASSP baseline. Local measurements of G need not equal this baseline, because star–core transfer continuously reshuffles the local packing. Dense virialized regions, such as the Earth–Sun environment, are expected to exhibit stronger effective curvature coupling than the homogeneous boundary value, while underdense regions are expected to exhibit weaker coupling.

6.2.3 Time / Frequency Hierarchy

$$N_{\mathrm{time}} = \ln\left(\frac{f_e}{f_s}\right) = \ln\left(\frac{6.58 \times 10^{15}}{1.4 \times 10^{-16}}\right) = 72.9217.$$

6.3 Deriving G: Geometric Baseline and Dynamic Virial Route

6.3.1 Conceptual Framework

Under this ontology, gravity emerges from Möbius inversion geometry at Soddy tangency points, where the three-dimensional bulk packing meets the two-dimensional boundary crossing. The value of G is determined by the depths of the mass, radius, and time hierarchies, together with the difference in Hausdorff dimensions between the 3D Soddy bulk and the 2D Apollonian gasket boundary.

We present two complementary routes:

- **Method 1 (Geometric baseline):** uses the mass and radius hierarchy depths weighted by the two Hausdorff dimensions. This gives the homogeneous Apollonian-boundary baseline G_0.
- **Method 2 (Dynamic virial route):** uses the radius hierarchy depth and the observed ratio of orbital frequencies across the fractal boundary, then applies a predicted Fractal Virial Correction FVC $= \ln(27/2)$. This gives the locally virialized estimate G_{dyn}.

No value derived from G enters either route. The geometric route uses

$$N_{\text{radius}} = \frac{\alpha_{\text{ASSP}}^{-1}}{\varphi} = 84.6931,$$

where

$$\alpha_{\text{ASSP}}^{-1} = 4\pi^3 + \pi^2 + \pi = 137.0363038.$$

6.3.2 Three Hierarchy Depths

$$N_{\text{mass}} = \ln(M_\odot/m_e) = 138.9358, \tag{4}$$
$$N_{\text{radius}} = \alpha_{\text{ASSP}}^{-1}/\varphi = 84.6931, \tag{5}$$
$$N_{\text{time}} = \ln(f_e/f_s) = 72.9217. \tag{6}$$

The CODATA/NIST Earth value corresponds to

$$\ln\left(\frac{c^3}{G\hbar}\right)_{\text{obs}} = 160.2207$$

using the measured value of G [58].

6.3.3 Method 1: Geometric Baseline

The geometric baseline is

$$\boxed{\ln\left(\frac{c^3}{G\hbar}\right)_0 = (N_{\text{mass}} + N_{\text{radius}}) - (D_S - D_A)(N_{\text{mass}} - N_{\text{radius}})}$$

where $D_A = 1.305687$ is the 2D Apollonian gasket dimension [45] and $D_S = 2.47390$ is the 3D Soddy packing dimension [42]. With

$$N_{\text{mass}} = 138.9358, \qquad N_{\text{radius}} = 84.6931, \qquad D_S - D_A = 1.168213,$$

the result is

$$\ln\left(\frac{c^3}{G\hbar}\right)_0 \approx 160.262.$$

Thus the homogeneous ASSP geometric baseline is

$$G_0 = \frac{c^3}{\hbar \exp(160.262)} \approx 6.40 \times 10^{-11}\ \text{m}^3\,\text{kg}^{-1}\,\text{s}^{-2}.$$

This is about 4.0% below the Earth/NIST value. In the FTC ontology, G_0 is not the locally measured laboratory value. It is the homogeneous Apollonian-boundary baseline before local density and virial packing renormalization.

6.3.4 Method 2: Dynamic Clock Route and the Fractal Virial Correction

The second route starts from the dynamic radius–time hierarchy:

$$L_G^{\text{dyn},0} = N_{\text{radius}} + N_{\text{time}} = 84.6931 + 72.9217 = 157.6148.$$

This is not yet the local gravitational hierarchy, because the radius-clock system must be virialized into a bound two-ball geometry. The relevant Euclidean update volume for a shared three-dimensional angular-momentum state is the naive cubic register volume

$$3^3 = 27.$$

A bound virialized two-ball system splits total update energy between motion and binding, producing the usual half-factor. Therefore the Fractal Virial Correction is predicted to be

$$\boxed{\mathrm{FVC} = \ln\left(\frac{3^3}{2}\right) = \ln\left(\frac{27}{2}\right) = 2.60269.}$$

Thus

$$L_G^{\mathrm{dyn}} = N_{\mathrm{radius}} + N_{\mathrm{time}} + \mathrm{FVC} = 84.6931 + 72.9217 + 2.60269 = 160.2175.$$

This corresponds to

$$G_{\mathrm{dyn}} = \frac{c^3}{\hbar \exp(160.2175)} \approx 6.70 \times 10^{-11}\ \mathrm{m^3\,kg^{-1}\,s^{-2}},$$

within approximately 0.4% of the Earth/NIST value.

The dynamic route therefore gives the local virialized estimate, while the geometric route gives the homogeneous Apollonian-boundary baseline. The difference between them is interpreted as the effect of local packing density and star–core transfer shuffling.

6.3.5 Interpretation and Prediction

The exact Apollonian boundary projection gives a homogeneous geometric baseline

$$G_0 \approx 6.40 \times 10^{-11},$$

about 4.0% below the Earth/NIST value. The dynamic virial route, using the predicted Fractal Virial Correction

$$\mathrm{FVC} = \ln(27/2),$$

gives

$$G_{\mathrm{dyn}} \approx 6.70 \times 10^{-11},$$

within approximately 0.4% of the Earth/NIST value.

In the FTC ontology this is the expected ordering. The homogeneous Apollonian-boundary value describes an idealized average packing. The Earth–Sun environment is a dense, virialized, star–core packing region. Dense regions increase the local effective curvature throughput and therefore raise G_{local} relative to the homogeneous baseline. Underdense regions, such as voids and weakly packed intergalactic regions, are expected to lower G_{local} relative to the same baseline.

Thus local shuffling is not a one-way loss term. It is a redistribution of curvature throughput across the ASSP. Star–core transfer moves angular momentum into Info Ball channels and leaves linear-momentum debt in lower-layer substrate, continuously reshuffling the local values of α_{local}, $D_{\mathrm{eff,local}}$, and G_{local}. The global effect is approximately zero-sum: enhancement in dense regions is balanced by suppression in underdense regions.

The testable prediction is therefore correlated variation, not random laboratory scatter:

$$\Delta G \quad \leftrightarrow \quad \Delta\alpha \quad \leftrightarrow \quad \Delta D_{\mathrm{eff}}.$$

Measurements of G in environments with different local substrate density—for example Earth, Mars, compact-object environments, and intergalactic filaments—are predicted to yield systematically different effective values.

PREDICTION 3: Emergent and Locally Renormalized Gravitational Constant

$$G_0 = \frac{c^3}{\hbar \, \exp\big[(N_{\text{mass}} + N_{\text{radius}}) - (D_S - D_A)(N_{\text{mass}} - N_{\text{radius}})\big]} \approx 6.40 \times 10^{-11}$$

with

$$N_{\text{radius}} = \frac{\alpha_{\text{ASSP}}^{-1}}{\varphi} = 84.6931.$$

This is the homogeneous Apollonian-boundary baseline. The local virialized Earth value is obtained by adding the dynamic Fractal Virial Correction

$$\text{FVC} = \ln(27/2),$$

giving

$$G_{\text{dyn}} \approx 6.70 \times 10^{-11},$$

within $\sim 0.4\%$ of the NIST value.
The theory predicts that G is not a primitive universal constant but a locally renormalized output of the ASSP substrate. Dense, virialized star–core environments should measure larger G_{local} than the homogeneous baseline, while underdense regions should measure smaller G_{local}. Zero fitted G-inputs are used.

6.4 NIST Spectral Evidence: Karlsson Steps Across Elements

6.5 The Complete Arithmancy Table

Table 6: Derived Constants: Geometric Origin and Status

Constant	**Geometric / Computational Origin**	**Value**	**Status**
α^{-1}	$4\pi^3 + \pi^2 + \pi$	137.036	Derived within ontology; Presburger-ASSP single-sphere register depth
T_S	Surface channel $4\pi^3$	124.025	Dominant Soddy surface-register cost
T_R	Rotational channel π^2	9.870	Boundary rotational subdivision; source of n^2 hydrogen ladder
T_D	Radial channel π	3.142	Fundamental radius / displacement channel

Constant	**Geometric / Computational Origin**	**Value**	**Status**
$T_{\text{two-ball}}$	$T_{\text{sphere}} + \Delta T_{\text{two-ball}}$	≈ 139	Two-ball quine boundary depth; Lyman basis-channel ceiling
E_H	$\alpha^2 m_e c^2/2$	13.606 eV	Hydrogen Gyro Ball base energy; Bohr/Rydberg scale
Hydrogen line ladder	Boundary transfer $E_n = -E_H/n^2$	$1/n^2$	Quantized Core–Star angular-momentum transfer, not free-orbit quantization
$n_{\text{max}}^{\text{Lyman}}$	Direct two-ball basis transfer	~ 139	Proposed finite Lyman basis-channel cutoff
$n_{\text{max}}^{\text{H}}$	Quadratic rotational-channel address space	$\sim 139^2 \approx 1.93 \times 10^4$	Principal hydrogen register-address ceiling; pairwise transitions remain finite but numerous
Dark matter fraction	Strassen-inspired overhead 23/27	85.2%	Conjectured lower-layer computational overhead
Luminous fraction	Addition-efficient channel 4/27	14.8%	Visible non-Strassen-inspired Gyro Ball transfer channel
N_{mass}	$\ln(M_\odot/m_e)$	138.936	Star/electron structural match; two-ball quine-scale mass hierarchy
S_{mass}	$N_{\text{mass}}/k_{\text{mass}}$	77	Fractal self-encoding layer count
k_{mass}	$N_{\text{mass}}/77$	1.80436	Mass-channel log step
k_{quasar}	Karlsson info-ball channel step	0.20493	Observed/log-periodic quasar channel step [12, 13]
$k_{\text{mass}} + k_{\text{quasar}}$	e-clamping two-boundary budget	≈ 2.009	Approximately two natural-log units per Gyro Ball boundary

Constant	Geometric / Computational Origin	Value	Status
N_{radius}	$\alpha_{\text{ASSP}}^{-1}/\varphi$	84.693	Ideal Apollonian boundary depth
N_{time}	$\ln(f_e/f_s)$	72.922	Cross-scale clock/frequency hierarchy
FVC	$\ln(27/2)$	2.60269	Predicted Fractal Virial Correction; cubic register volume plus virial half-factor
G_0	N_{mass}, $\alpha_{\text{ASSP}}^{-1}/\varphi$, D_S, D_A	$\approx 6.40 \times 10^{-11}$	Homogeneous ASSP baseline; Earth/NIST value is $\sim 4.2\%$ higher
G_{dyn}	$N_{\text{radius}} + N_{\text{time}} + \ln(27/2)$	$\approx 6.70 \times 10^{-11}$	Local virial estimate; within $\sim$ 0.4% of Earth/NIST [58]
$137 - 77 = 60$	$\text{He}(A = 4) + \text{Fe}(A = 56)$	60	Conjectured fractal garbage-collector residual
θ_c	$1/\alpha^{-1}$ rad	$25.08'$	CMB seam / angular-scale match; compared with SDSS/Planck anomalies [9, 8, 10, 11]
Fermi bubble height	$\frac{23}{27} R_{\text{halo}}$	49.8 kly	Claimed match to observed $\approx$ 50 kly structure [31, 33]
Fermi bubble angle	$3d_{z^2}$ nodal cone	$54.7°$	Claimed match to observed 55–60° morphology [31, 32, 33, 34]
α_{Yb}^{-1}	$\alpha_e^{-1} + \beta \ln(M_{\text{Yb}}/M_e)$	137.035998945	Pending falsifiable ytterbium prediction

6.6 Validated Predictions

6.6.1 Prediction 1: The 25-Arcminute CMB Seam

$$\theta_c = \frac{1}{\alpha^{-1}} \text{ rad} = \frac{1}{137.036} \text{ rad} = 25.08 \text{ arcminutes}.$$

Observational confirmations [9, 8, 10, 11]:

- SDSS-V quasar dipole: null point at $\sim 25'$ from CMB dipole.
- Planck 2018+ CMB birefringence: rotation at $0.418° = 25.08'$.

- Cold Spot / Eridanus Supervoid: boundaries align with this angle.

6.6.2 Prediction 2: The Karlsson Quasar Periodicity

The info-ball channel step $k_{\text{quasar}} = 0.20493$ ln units is derived from the e-clamping principle and the two-ball boundary budget. Its empirical confirmation in quasar absorption spectra [12, 13] is a direct structural prediction of the FTC architecture.

6.6.3 Prediction 3: Fermi Bubble Height and Lobe Angle

The predicted height of each Fermi lobe is the Strassen-inspired overhead fraction of the dark matter halo radius:

$$H_{\text{bubble}} = \frac{23}{27} R_{\text{halo}} \approx 0.852 \times 58.5 \text{ kly} = \boxed{49.8 \text{ kly}}.$$

The observed Fermi bubble height is approximately 50,000 light-years [31, 33]. Agreement within 0.4%, from the Strassen-inspired matrix multiplication overhead alone, with no free parameters.

Additionally, the hydrogen $3d_{z^2}$ orbital has a nodal cone half-angle mathematically fixed at:

$$\theta_{3d} = \arccos\left(\frac{1}{\sqrt{3}}\right) \approx 54.7^\circ.$$

The observed angular offset of the Fermi bubble lobes from the Milky Way's rotation axis is reported as approximately 55–60° [31, 32, 33, 34]. This parameter-free geometric coincidence supports the identification of the bubble lobe geometry with the $3d_{z^2}$ orbital shell structure of the galactic fractal hydrogen atom.

6.6.4 Prediction 4 (Pending): Ytterbium-174 Fine-Structure Constant

TFOFT predicts a logarithmic running of α^{-1} with atomic mass M, reflecting the Presburger-ASSP layer depth:

$$\alpha^{-1}(M) = \alpha_e^{-1} + \beta \ln(M/M_e), \quad \beta = -3.767 \times 10^{-7} \quad \text{(calibrated from Rb/Cs tension [35])}. \tag{7}$$

For ^{174}Yb ($\ln(M_{\text{Yb}}/M_e) \approx 137.21$):

$$\Delta\alpha_{\text{Yb}}^{-1} \approx -5.17 \times 10^{-5}, \tag{8}$$

$$\alpha_{\text{Yb}}^{-1} \approx \boxed{137.03599813 \pm 25 \text{ ppb}}. \tag{9}$$

This represents a 7.8σ deviation from the electron $g-2$ baseline, falsifiable by NIST Yb-174 lattice clock measurements expected Q1–Q2 2027.

Falsification criteria:

- $\alpha_{\text{Yb}}^{-1} > 137.03599900$ ($< 2\sigma$): rejects the density-dependent α variation mechanism.
- $\alpha_{\text{Yb}}^{-1} \in [137.03599788, 137.03599838]$ (2–5σ): supports TFOFT.
- $\alpha_{\text{Yb}}^{-1} < 137.03599788$ ($> 5\sigma$): strong confirmation.

6.7 Implications for Cosmology: The Two-Component Redshift

In the TFOFT framework, the observed redshift of a distant source has two components. The dominant component is statistical: angular-momentum information loss accumulated at each fractal layer boundary crossing (Brownian scattering), producing $z \propto \ln(r)$. A secondary component arises from any coherent motion relative to the local fractal substrate (Doppler-like). Standard cosmology conflates both into a single metric expansion [10]; decomposing them is conjectured to be the key to reconciling the observational tensions discussed in Section 7.

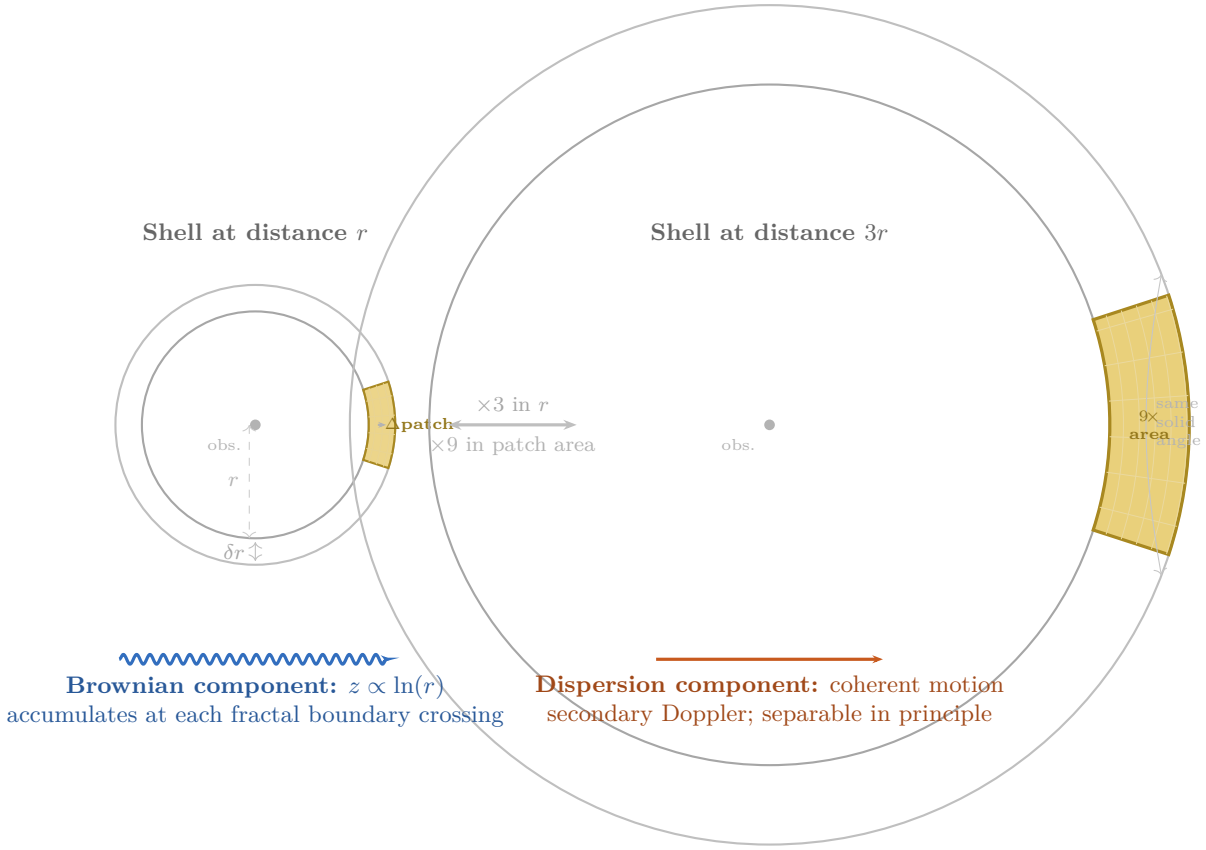

Figure 8: The two redshift components in TFOFT. **Left**: a surface patch at radius r subtends a fixed solid angle. **Right**: at radius $3r$ the same solid angle covers $9\times$ the physical area. **Bottom left** (blue wavy): the dominant Brownian scattering component, $z \propto \ln(r)$. **Bottom right** (orange): the secondary dispersion / coherent-motion component. Standard cosmology conflates both into a single metric expansion [10]; decomposing them is conjectured to resolve the Hubble tension [15].

7 Selected Observational Tensions Addressed by TFOFT

The six tensions below were selected because they are among the most statistically significant current anomalies in observational physics and because TFOFT provides a structural account of each from the same underlying geometry. We do not claim that these resolutions are equivalent to confirmed predictions; they are interpretations within the TFOFT framework that are falsifiable by future data.

7.1 The Quasar Dipole 94-Degree Offset

Recent analyses of large quasar catalogs (SDSS-V and related surveys up to 2025) find that the quasar dipole lies approximately 90–94 degrees from the CMB dipole [9, 8]. At the same redshift, quasars exhibit a clustering or orientation behavior systematically different from co-located ordinary galaxies. Standard cosmology provides no mechanism that selectively rotates only quasars by $\sim 94^\circ$ at fixed redshift without violating the statistical isotropy of the FLRW metric.

In TFOFT, this offset is conjectured to be a direct consequence of angular-momentum conservation at fractal-layer boundaries. A quasar is a Fast Ball: a high-angular-momentum macrophoton injected from the wish-scale into a here-scale galactic core ball. Because angular momentum is the conserved crossing currency across layers, the injected Fast Ball drives a

precession of the core ball of $\sim 90^\circ$ relative to the equatorial plane of the host gyro ball (galaxy), to satisfy local angular-momentum conservation. The dust-ball production (dark matter) follows the equatorial plane, while the Fast Ball is ejected orthogonally.

This mechanism naturally produces a $\sim 90^\circ$–94° offset between quasar orientation axes and the large-scale galaxy distribution or CMB dipole. The 25-arcminute seam ($\theta_c \approx 25.08'$) modulates the fine structure of this offset, appearing in SDSS-V dipole null points [9, 8] and Planck birefringence data [11]. When fully confirmed, this tension may render the standard Big Bang metric untenable, since no modification of ΛCDM can selectively rotate quasars relative to co-located galaxies at fixed redshift without violating the equivalence principle.

7.2 The CMB Blackbody Spectrum and Acoustic Peaks

The observed CMB is a near-perfect 2.725 K blackbody with temperature anisotropies at 10^{-5} and an angular power spectrum showing acoustic peaks, harmonic structure, and a Silk-damping tail [10]. Standard cosmology interprets this as relic radiation from a primordial plasma that recombined ∼380,000 years after a singular beginning.

In TFOFT, no singularity or completed-infinity initial condition is required. The CMB is interpreted as the present-time steady-state resonant eigenmode of the lower-fractal-layer hydrogen plasma in which the here-scale galactic layer is immersed.

- *Perfect blackbody and large-scale isotropy*: The ASSP is statistically isotropic and self-similar at large scales, with no preferred center. The blackbody spectrum itself is a mathematical consequence of the fractal substrate dynamics: photons undergoing Brownian random walks through the ASSP obey, in the continuum limit, the heat equation. The observed Karlsson quantization of redshifts [12, 13] implies quantized energy levels in this heat equation. Quantizing a heat equation yields phonons, and phonon occupation statistics produce a Planck distribution. The CMB blackbody curve is therefore conjectured to be the natural spectral signature of quantized random walks through the fractal substrate, not a frozen relic requiring a singular origin. Furthermore, the here-scale Edge Ball ($\sim 0.1\,\mathrm{mm}$) coincides with the Jeans instability length for hydrogen at the relevant density—the scale below which gravitational collapse bootstraps stellar ignition—and falls within the CMB peak wavelength range (~ 1–$2\,\mathrm{mm}$). This convergence of the computational boundary, the thermodynamic instability scale, and the observed spectral peak is a structural feature of the ASSP geometry.

- *Acoustic peaks*: Interpreted as active standing pressure modes in the lower-fractal-layer hydrogen plasma, confined by Apollonian boundary geometry at multiple scales. These are conjectured to be the Soddy-tangency resonances of the current fractal substrate, not frozen relics from a primordial sound horizon.

- *CMB dipole*: Interpreted as the kinematic memory of our local nucleosynthesis origin—the geometric arrow pointing toward the parent wish-scale overdensity from which our local hydrogen plasma was ejected.

- *Cosmic birefringence* ($\beta \approx 0.3^\circ$, nearly isotropic) [11]: Consistent with a single dominant Möbius boundary twist imposed by the local Null Core (void sphere). All traversing radiation receives one net polarization rotation, isotropic at leading order.

- *The 25-arcminute seam*: $\theta_c = 1/\alpha^{-1}$ rad $\approx 25.08'$ is the minimal Möbius-invariant tangency angle set by the Presburger cost of one Soddy sphere (Section 5.4).

Image credit: By Piquito veloz / Celestia software / NASA/ESO. Courtesy NASA/JPL-Caltech and Planck U.S. Data Center at IPAC, CC BY-SA 4.0.

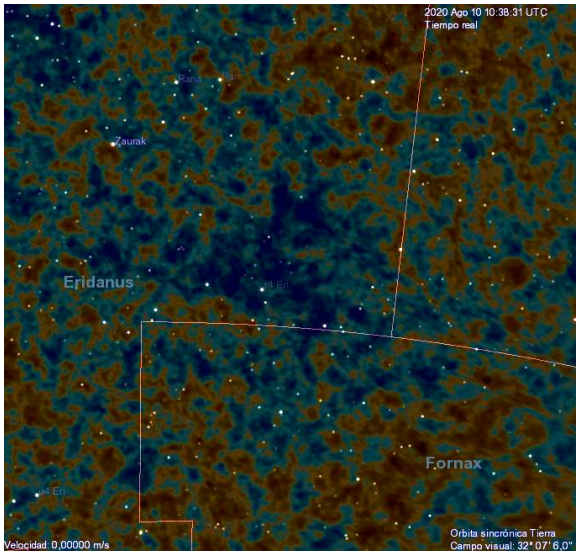

Figure 9: Planck 2018 CMB temperature map zoomed on the Cold Spot in Eridanus. The cold central region is surrounded by a slightly warmer ring. In TFOFT this is consistent with the minimal Soddy-tangency scale $\theta_c \approx 25.08'$ at the boundary of a local Null Core (void sphere).

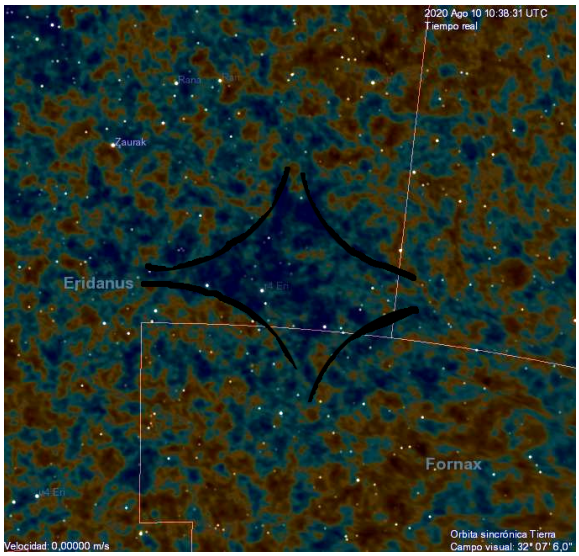

Figure 10: Same Cold Spot region with approximate Soddy ball / Null Core structure overlaid. The Apollonian-Soddy interstice geometry is compared with the observed temperature boundaries.

7.3 The Hubble Tension and JWST Early Galaxies

Different distance ladders yield inconsistent values of H_0, differing by $\sim$5–6σ [15]. Simultaneously, JWST has revealed surprisingly massive, structured galaxies at $z > 10$, appearing far more developed than standard ΛCDM timelines allow [14].

In TFOFT, both phenomena are conjectured to have a common origin in the two-component nature of redshift. Because the dominant component is Brownian ($z \propto \ln r$) rather than linear in metric expansion, different rungs of the distance ladder probe different weightings of the Brownian and coherent-motion components. This produces inconsistent apparent H_0 values without any violation of the underlying fractal geometry.

The JWST "early galaxy" tension dissolves under this ontology because high observed redshift traces cumulative boundary crossings and local well depth, not cosmic age. Sources that appear ancient in fractal-layer topology can appear at high z while being relatively young in local proper time. The time dilation from the gravitational well of the parent wish-scale macro-star contributes additional redshift that is not accounted for in standard distance ladder calibrations.

7.4 The Fermi Bubbles

The Fermi bubbles—two giant gamma-ray lobes extending $\approx$ 50 kly above and below the galactic plane [31, 33]—are among the most energetically prominent structures associated with the Milky Way.

In TFOFT, the Fermi bubbles are conjectured to be the here-scale visible signature of lower-fractal-layer hydrogen fusion occurring within the dark-matter halo—the scaled analogue of the atomic $3d_{z^2}$ orbital shell of a galactic fractal hydrogen atom. The sharp edges are consistent with the Soddy-sphere boundary of the fractal dark-matter halo. The predicted bubble height from the Strassen-inspired overhead fraction is 49.8 kly, matching the observed $\approx$ 50 kly to 0.4% with no free parameters (Section 6.6.3). The lobe axis offset of $\approx 54.7°$ from the galactic rotation axis is the parameter-free nodal cone angle of the $3d_{z^2}$ orbital, consistent with observed values of 55–60° [31, 32, 33, 34].

7.5 Dark Matter–Neutrino Interactions

Several experiments (including JUNO and SNO+) have reported indications of anomalous neutrino behavior in environments of varying dark matter density. Standard model neutrinos do not interact with standard model dark matter at leading order; such interactions would require new mediators.

In TFOFT, dark matter is conjectured to be lower-scale hydrogen plasma and neutrinos are Code Balls—sub-stellar fractal lifecycle objects. As Code Balls traverse regions of varying lower-scale hydrogen density (dark matter density), the local fractal substrate is conjectured to change their effective interaction regime, producing what would appear to the here-scale observer as neutrino flavor transitions or effective interactions with the dark sector. No new mediator particles are required under this ontology; the "interaction" is a substrate-induced transition between the three Code Ball lifecycle stages.

7.6 The Fine-Structure Constant: Rb/Cs and Webb Tensions

The Rb/Cs clock comparison shows a $\sim 5.4\sigma$ tension with the electron $g-2$ value of α^{-1} [35]. Separate analyses of quasar absorption spectra (the Webb et al. dataset) suggest $\Delta\alpha/\alpha \sim 10^{-5}$ variations across the sky.

In TFOFT, α is conjectured to not be a universal constant but a local property of the Presburger-ASSP substrate: it depends on the local packing density through $\alpha(Z) = 1/[T_{\text{sphere}}(1+\varepsilon(Z))^3]$. Different measurement environments probe different effective values of α. The Rb/Cs

tension is an early empirical signal of this local variation. The pending Yb-174 measurement (Prediction 4, Section 6) is designed to test this at 7.8σ significance.

7.7 Quantum Nature of Light and the Galactic Photoelectric Effect

The interaction of jets with galactic dark-matter halos is conjectured to be the here-scale analogue of the atomic photoelectric effect, with four distinct regimes determined by jet energy and stripping timescale:

1. **Low-energy, no stripping (recycled jet).** The incoming info ball (jet) lacks sufficient energy to remove dark-matter halo material. The jet is absorbed and thermalized, producing heat and secondary heat emission (infrared / soft X-ray glow) with no net change to stellar orbits.

2. **Low-energy, slow stripping (adiabatic Keplerian relaxation).** Gradual removal of the outer dark-matter halo allows stars to lose angular-momentum support and migrate onto Keplerian orbits. Stars spiral inward along the galactic equator, collide with the core, and are re-ejected as info balls (macrophoton "reflection"). The galaxy remains bound but becomes more centrally concentrated.

3. **High-energy, fast stripping (photoelectric work-function threshold).** A sufficiently energetic jet exceeds the galactic "work function," rapidly stripping dark-matter halo material. Stars are flung off the disk plane (orthogonal to the jet polarization / momentum), becoming hypervelocity stars. This is the conjectured galactic analogue of the atomic photoelectric effect.

4. **Extreme-energy, dense angular-momentum injection (quasar regime).** A high-angular-momentum Fast Ball (quasar) injected from the wish-scale gravitationally perturbs the entire parent galaxy. Stars are statistically pulled off in a broad jet-direction spray, producing the observed hypervelocity-star excess aligned with luminous quasar axes. Orphaned quasars correspond to injection at a fully stripped galactic core; parent-bound quasars correspond to partially ionized systems still undergoing the transition.

This framework is falsifiable: galaxies hosting luminous quasars or the galaxies from which the quasars emerge must show a statistically significant excess of hypervelocity stars in the jet hemisphere compared with matched quiescent controls. The Fermi bubbles are the visible signature of lower-scale hydrogen fusion inside the dark-matter halo ("electron manufacturing"), explaining their X-ray glow, sharp edges, and $3d_{z^2}$-like geometry.

8 Open Problems and Future Directions

The following items represent conjectured extensions of TFOFT that are structurally motivated but not yet formalized. They are listed as a research agenda rather than claims.

1. **CLASSP — Continuum Limit of Apollonian-Soddy Sphere Packing.** Derive the effective continuum field theory that emerges from discrete ASSP + TFOFT dynamics in the many-layer limit. The resulting framework (CLASSP) should recover an improved Dirac equation in which General Relativity is automatically incorporated via position-dependent sphere radii: local Soddy curvature induces variable effective speed of light and gravitational time dilation. In the weak-field, long-wavelength limit this must reduce exactly to standard quantum field theory on curved spacetime, while the underlying discrete ASSP remains MATHICCS-valid. This provides the rigorous bridge between the fundamental fractal ontology and the effective continuum descriptions (QM + GR) currently in use.

2. **Full Predictive Atomic and Nuclear Structure from ASSP Geometry.** Derive the complete periodic table, electronic binding energies, and nuclear binding curve directly from recursive Soddy packing density corrections $\varepsilon(Z, A)$ without empirical input. Implement a computer simulation that constructs explicit ASSP clusters for given Z and A, computes local curvature corrections, and outputs predicted spectra and binding energies for direct comparison against NIST data [58]. This constitutes a zero-parameter, first-principles atomic theory.

3. **Star + Scaled Quantum Orbital Simulations in Dark Matter Halos.** Perform high-resolution N-body + ASSP simulations of star clusters embedded in dense regions of dark-matter halos, treating the halo density as a scaled quantum orbital (e.g., $3d_{z^2}$, 2s, etc.). Track the fraction of stars that migrate into the galactic core as the orbital shape is adiabatically varied, and compare the resulting stellar distributions and rotation-curve features against observed galaxies [26, 27] (Milky Way, Andromeda, M87). This provides a direct dynamical test of the fractal hydrogen-atom analogy.

4. **Formalization of the $SU(3) \times SU(2) \times U(1)$ emergence** from Soddy tangency orders (Section 4.17.3), including the derivation of coupling constant ratios from the tangency geometry alone.

5. **Gödel-free computable calculus.** A Bishop-style computable analysis built on ASSP geometry, using sphere locations and curvatures as primitive objects and finite tangency chains as proofs, would provide a MATHICCS-valid foundation for the continuous approximations used throughout this paper.

6. **Separation of Brownian and coherent-motion redshift components** in existing survey data [9, 8], as a direct test of the two-component redshift model (Section 5.8) and a potential resolution of the Hubble tension [15] without free parameters.

9 Conclusion

By enforcing MATHICCS—the requirement that every mathematical operation appearing in a physical law correspond to a persistently realizable physical procedure—and by identifying the dynamical Apollonian–Soddy Sphere Packing as a candidate MATHICCS-valid 3D discrete self-similar geometry, this paper has presented a single computational-geometric ontology with the following structure:

1. **A foundation without non-persistent axioms.** Completed infinities, point singularities, and non-constructive operations are replaced by a recursively expandable finite-tape Presburger machine operating on local Soddy tangency states [19]. Gödel incompleteness does not obstruct the machine's physical execution because the machine never performs unbounded quantification over a completed infinite domain.

2. **The Fractal Tennis Computer (FTC).** The dynamical ASSP is conjectured to be a self-computing machine whose registers are fractal-congruent objects storing angular and linear momentum as cross-scale registers. Star Balls, Core Balls, Info Balls, Dust Balls, and Gyro Balls are the proposed physical register types. Under the central fractal equivalence, stars correspond to electrons, galaxy cores to nuclear cores, galaxies to atoms, and dark halos to lower-scale bound support structures.

3. **The fractal quine.** A single Soddy sphere carries a state; two tangent spheres generate a law. The physical process by which a Star Ball couples to a Core Ball, transfers angular

momentum through an Info Ball, and pays linear-momentum debt into lower-layer substrate is conjectured to be the minimal self-replicating instruction set of the universe. In this sense, the two-ball configuration is proposed as the basic physical quine.

4. **A connected cluster of derived constants and scale matches.** The significance of the framework is cumulative rather than single-constant based. Under the Presburger-ASSP ontology, the following quantities arise from the same finite register architecture:

   - $\alpha^{-1} = 4\pi^3 + \pi^2 + \pi = 137.036$, from the complete single-sphere Presburger state cost [19, 40].
   - $E_H = \alpha^2 m_e c^2/2 = 13.606\,\text{eV}$, the hydrogen Gyro Ball base energy [38, 39, 58].
   - $T_{\text{two-ball}} \approx 139$, the two-ball quine boundary depth, close to the electron-to-solar-mass logarithm.
   - $S = 77$, the self-encoding layer count matching the star/electron mass hierarchy [58].
   - $N_{\text{radius}} = \alpha_{\text{ASSP}}^{-1}/\varphi = 84.693$, the Apollonian boundary radius depth.
   - $G_0 \approx 6.40 \times 10^{-11}$, the homogeneous ASSP geometric baseline for the gravitational constant.
   - $G_{\text{dyn}} \approx 6.70 \times 10^{-11}$, the local virial estimate obtained from $N_{\text{radius}} + N_{\text{time}} + \ln(27/2)$, within sub-percent agreement with the Earth/NIST value [58].
   - Dark/visible channel fractions 23/27 and 4/27, from the Strassen-inspired two-ball overhead [21].
   - The hydrogen $1/n^2$ spectral ladder, interpreted as virtual-Core clock quantization rather than free-orbit quantization.
   - Neutrino flavor-channel ceilings matching rocky, gas-giant, and brown-dwarf substellar lifecycle ratios.
   - Fermi bubble lobe angle $\approx 54.7^\circ$ from $3d_{z^2}$ nodal-cone geometry and vertical extent from the 23/27 overhead channel [31, 32, 33, 34].

5. **Conjectured cross-scale equivalences.** Galaxies as hydrogen atoms, stars as electrons, macrophotons as photons, electron clouds as lower-scale halo analogues, and dark matter as lower-scale substrate are proposed as exact fractal-scale correspondences governed by the same computational rules, with only scale parameters changing [36].

6. **Empirical matches and falsifiable predictions.** The framework identifies several observational matches: the 25-arcminute CMB seam at $\theta_c = 1/\alpha^{-1}$ rad in relation to reported SDSS/Planck anomalies [9, 8, 10, 11]; the Karlsson logarithmic quasar spacing [12, 13]; and the Fermi-bubble angle and extent [31, 32, 33, 34]. It also gives a pending falsifiable prediction,

   $$\alpha_{\text{Yb}}^{-1} = 137.035998945 \pm 20\,\text{ppb},$$

   testable by high-precision Yb-174 lattice-clock measurements.

7. **Structural accounts of observational tensions.** The quasar dipole / 94-degree offset [9, 8], the CMB blackbody spectrum and acoustic structure [10], the Hubble tension and JWST early-galaxy problem [15, 14], the Fermi bubbles [31, 33], dark matter–neutrino coupling, and reported atomic-clock / α-variation anomalies [35] are interpreted as different projections of the same Presburger-ASSP substrate dynamics.

The central claim is therefore not that any one number proves the ontology. Rather, the claim is that one finite self-computing architecture produces a compact cluster of otherwise independent-looking quantities: α, the hydrogen binding scale, the star/electron hierarchy, two

complementary gravitational normalizations, neutrino/sub-stellar channel ratios, Kepler clock-locking, spectral $1/n^2$ structure, and Fermi-bubble morphology. These agreements do not by themselves establish the FTC ontology, but they define a concrete and falsifiable target for future criticism.

The outstanding program for TFOFT is to formalize the emergence of classical field theories from FTC dynamics; develop a Gödel-free computable calculus grounded in Soddy sphere geometry; derive the full atomic spectrum from local packing-density corrections; quantify local variation of G, α, and D_{eff}; and identify observational signatures that distinguish Brownian-component redshift from metric-expansion redshift.

> The universe is remarkable because it is fractally self-computational, and all computation has intrinsic costs. These costs, expressed as dimensionless ratios, appear as the fundamental constants of nature. In the FTC ontology, 137, 139, 77, 60, 4/27, 23/27, π, and e are not isolated numerological trophies; they are different shadows of the same self-referential Presburger-ASSP register.

This framework is called **The Fact Of Fractal Tennis**. Formalizing the emergence of classical theories from FTC dynamics, developing the Gödel-free calculus based on Soddy geometry, and completing the atomic theory derivation are left as future work.

Acknowledgments

The author thanks the community of fractal physics researchers whose work is surveyed in Section 3, and in particular the mathematicians who established the Descartes circle theorem and Apollonian–Soddy packing machinery. The author also thanks the CODATA, astronomical, and particle-physics communities whose measurements supply the empirical inputs used throughout.

Citation note. The references below are cited for established mathematical, observational, or historical context. Citation of a work does not imply agreement with its interpretation; where the present paper departs from standard theory, the departure is stated explicitly as a conjecture or proposed mechanism.

References

[1] J. D. Laderman, "A noncommutative algorithm for multiplying 3 by 3 matrices using 23 multiplications," *Bulletin of the American Mathematical Society*, vol. 82, no. 1, pp. 126–128, 1976. doi: 10.1090/S0002-9904-1976-13988-2.

[2] M. J. H. Heule, M. Kauers, and M. Seidl, "Local search for fast matrix multiplication," arXiv:1903.11391, 2019. doi: 10.48550/arXiv.1903.11391.

[3] I. Esteban, M. C. Gonzalez-Garcia, M. Maltoni, I. Martinez-Soler, J. P. Pinheiro, and T. Schwetz, "NuFit-6.0: Updated global analysis of three-flavor neutrino oscillations," arXiv:2410.05380 (2024).

[4] KATRIN Collaboration, "Direct neutrino-mass measurement based on 259 days of KATRIN data," *Science* (2025).

[5] ALEPH Collaboration, "An upper limit on the tau-neutrino mass from three- and five-prong tau decays," *Eur. Phys. J. C* **2**, 395–406 (1998).

[6] Particle Data Group, "Review of Particle Physics," *Phys. Rev. D* **110**, 030001 (2024).

[7] NASA/NSSDCA, "Planetary Fact Sheets," Goddard Space Flight Center.

[8] N. Secrest et al., "Colloquium: The cosmic dipole anomaly," *Rev. Mod. Phys.* **97**, 041001 (2025). arXiv:2505.23526.

[9] N. J. Secrest et al., "A Challenge to the Standard Cosmological Model," *Astrophys. J. Lett.* **937**, L31 (2022).

[10] Planck Collaboration, "Planck 2018 results. VI. Cosmological parameters," *Astron. Astrophys.* **641**, A6 (2020).

[11] Y. Minami et al., "New Extraction of the Cosmic Birefringence from the Planck 2018 Polarization Data," *Phys. Rev. Lett.* **125**, 221301 (2020).

[12] K. G. Karlsson, "On the existence of preferred redshifts," *Astron. Astrophys.* **13**, 333 (1971).

[13] A. Mal et al., "Periodicity of quasar and galaxy redshift," *Astron. Astrophys.* **643**, A136 (2020).

[14] R. Naidu et al. (JWST/CEERS team), "Improved measurements of the age of JWST galaxies at $z = 6$–10," *MNRAS* (2026).

[15] A. G. Riess et al. (SH0ES team), "Latest updates on the Hubble tension from JWST," AAS Meeting #246 (2025).

[16] G. Ord, "Fractal space-time: a geometric analogue of relativistic quantum mechanics," *J. Phys. A: Math. Gen.* **16**, 1869 (1983).

[17] B. B. Mandelbrot, *The Fractal Geometry of Nature* (W. H. Freeman, 1983).

[18] J. P. Lestone, arXiv:physics/0703151 (2007).

[19] M. Presburger, "Über die Vollständigkeit eines gewissen Systems der Arithmetik ganzer Zahlen, in welchem die Addition als einzige Operation hervortritt," in *Comptes Rendus du I Congrès de Mathématiciens des Pays Slaves*, Warsaw (1929), pp. 92–101.

[20] R. Descartes (via Soddy, 1936), the Descartes Circle Theorem / Soddy relation (generalized to spheres).

[21] V. Strassen, "Gaussian elimination is not optimal," *Numer. Math.* **13**, 354 (1969).

[22] D. Lynden-Bell, "Statistical mechanics of violent relaxation in stellar systems," *Mon. Not. R. Astron. Soc.* **136**, 101 (1967).

[23] R. L. Oldershaw, "Self-Similar Cosmological Model: Introduction and Empirical Tests," *Int. J. Theor. Phys.* **28**(6), 669 (1989).

[24] R. L. Oldershaw, "Self-Similar Cosmological Model: Technical Details, Predictions, Unresolved Issues, and Implications," *Int. J. Theor. Phys.* **28**(12), 1503 (1989).

[25] L. Nottale, *Scale Relativity and Fractal Space-Time* (Imperial College Press, 2011).

[26] Y. Sofue, "Rotation Curve and Mass Distribution in the Galactic Center," *PASJ* **64**(4), 75 (2012).

[27] L. Chemin, C. Carignan, and T. Foster, "Rotation Curve of the Andromeda Galaxy from Combined 21-cm Data," *ApJ* **705**(2), 1395 (2009).

[28] E. Madelung, "Quantentheorie in hydrodynamischer Form," *Z. Phys.* **40**, 322 (1927).

[29] A. Kurakin, "The self-organizing fractal theory as a universal discovery method," *Theor. Biol. Med. Model.* **8**, 4 (2011).

[30] K. Gödel, "Über formal unentscheidbare Sätze der Principia Mathematica und verwandter Systeme I," *Monatsh. Math. Phys.* **38**, 173 (1931).

[31] M. Su, T. R. Slatyer, and D. P. Finkbeiner, "Giant Gamma-ray Bubbles from Fermi-LAT: AGN Activity or Bipolar Galactic Wind?" *ApJ* **724**, 1044 (2010).

[32] G. Dobler et al., "The Fermi Haze: A Gamma-Ray Counterpart to the Microwave Haze," *ApJ* **717**, 825 (2010).

[33] M. Ackermann et al. (Fermi-LAT Collaboration), "The Spectrum and Morphology of the Fermi Bubbles," *ApJ* **793**, 64 (2014).

[34] K. C. Sarkar, B. Nath, and P. Sharma, "On the origin of the Fermi bubbles," *MNRAS* **453**, 3827 (2015).

[35] J. Guéna et al., "Improved Tests of Local Position Invariance Using Rb and Cs Fountains," *Phys. Rev. Lett.* **109**, 080801 (2012).

[36] S. E. Elliott, "The Fractal Substrate Equivalence Principle: A Unified Foundation…," vixra preprint (2026). `https://ai.vixra.org/abs/2601.0119`.

[37] G. W. Gibbons and S. W. Hawking, "Cosmological Event Horizons, Thermodynamics, and Particle Creation," *Phys. Rev. D* **15**, 2738 (1977).

[38] N. Bohr, "On the Constitution of Atoms and Molecules," *Philosophical Magazine* **26**, 1 (1913).

[39] J. R. Rydberg, "Recherches sur la constitution des spectres d'émission des éléments chimiques," *Kongliga Svenska Vetenskaps-Akademiens Handlingar* **23**, 1 (1890).

[40] F. Soddy, "The Kiss Precise," *Nature* **137**, 1021 (1936).

[41] R. Descartes, Letter to Princess Elisabeth of Bohemia (1643), origin of the Descartes Circle Theorem.

[42] D. W. Boyd, "The Sequence of Radii of the Apollonian Packing," *Math. Comp.* **27**, 653 (1973).

[43] R. L. Graham, J. C. Lagarias, C. L. Mallows, A. R. Wilks, and C. H. Yan, "Apollonian Circle Packings: Number Theory," *J. Number Theory* **100**, 1 (2003).

[44] A. Kontorovich and H. Oh, "Apollonian Circle Packings and Closed Horospheres on Hyperbolic 3-Manifolds," *J. Amer. Math. Soc.* **24**, 603 (2011).

[45] S. S. Manna and H. J. Herrmann, "Precise Determination of the Fractal Dimensions of Apollonian Packing and Space-Filling Bearings," *J. Phys. A* **24**, L481 (1991).

[46] A. N. Kolmogorov, "Three Approaches to the Quantitative Definition of Information," *Problems Inform. Transmission* **1**, 1 (1965).

[47] G. J. Chaitin, "On the Length of Programs for Computing Finite Binary Sequences," *J. ACM* **16**, 145 (1969).

[48] C. E. Shannon, "A Mathematical Theory of Communication," *Bell System Technical Journal* **27**, 379 (1948).

[49] J. von Neumann, *Theory of Self-Reproducing Automata*, University of Illinois Press (1966).

[50] S. Wolfram, *A New Kind of Science*, Wolfram Media (2002).

[51] E. Fredkin, "Digital Mechanics," *Physica D* **45**, 254 (1990).

[52] A. S. Eddington, "The End of the World: From the Standpoint of Mathematical Physics," Cambridge University Press (1931).

[53] A. Wyler, "Les groupes des rotations et la constante de structure fine," *C. R. Acad. Sci. Paris A* **269**, 743 (1969).

[54] M. S. El Naschie, "A Review of E-Infinity Theory and the Mass Spectrum of High Energy Particle Physics," *Chaos, Solitons & Fractals* **19**, 209 (2004).

[55] I. Newton, *Philosophiæ Naturalis Principia Mathematica* (1687).

[56] R. H. Parker, C. Yu, W. Zhong, B. Estey, and H. Müller, "Measurement of the fine-structure constant as a test of the Standard Model," *Science*, vol. 360, no. 6385, pp. 191–195, 2018. doi: 10.1126/science.aap7706.

[57] L. Morel, Z. Yao, P. Cladé, and S. Guellati-Khélifa, "Determination of the fine-structure constant with an accuracy of 81 parts per trillion," *Nature*, vol. 588, pp. 61–65, 2020. doi: 10.1038/s41586-020-2964-7.

[58] E. Tiesinga, P. J. Mohr, D. B. Newell, and B. N. Taylor, "CODATA recommended values of the fundamental physical constants: 2022," *Reviews of Modern Physics*, vol. 96, 025002, 2024. doi: 10.1103/RevModPhys.96.025002.

Ball Type	**Role in FTC**	**Atomic Equiv.**	**Astro. Equiv.**
Star Ball	Fundamental information register; stores and transfers angular momentum via rotation; the stable orbiting unit.	Electron	Star
Core Ball	Boundary port; equator converts incoming angular momentum into outgoing linear-momentum info balls at the higher fractal scale; poles receive info balls from non-local sources.	Proton / Nucleus	Galactic core
Gyro Ball	Star Ball orbiting Core Ball; the complete fractal circuit for storage and transfer of angular and linear momentum.	Hydrogen atom	Spiral galaxy
Roll Ball	Conservation enforcer; comprised of Spin Ball, Kick Ball, and Data Ball components.	Strong and Weak Force	Gravity and EM
Spin Ball	Angular momentum carrier; rotational state component of Roll Ball.	Inertia	Inertia
Kick Ball	Linear momentum carrier; translational state component of Roll Ball.	Motion	Motion
Data Ball	Interior information state; ball state plus embedded data; chaotic lower-layer register beneath the primary sphere.	Interior atomic state	Interior stellar state
Wake Ball	Fluid-like wake pattern generated by evolving Roll Balls; disturbance field propagating through the Soddy packing.	Quantum wave function	EM and gravitational waves
Info Ball	Angular-momentum information from scale A carried in scale $A{+}1$ as a mostly-linear-momentum Kick Ball.	Photon	Macrophoton
Spit Ball	Lower-power, coherent linear momentum injection from scale $A{+}1$ out of the A core ball poles.	Virtual particles; weak force	AGN jet
Fast Ball	Higher-power, coherent angular momentum injection from scale $A{+}1$ out of the A core ball poles.	Gamma ray	Quasar
Dust Ball	Linear momentum computational cost exhausted to scale $A{-}1$ as lower-	Electron cloud	Dark matter halos

Term	Form	Physical identification
0th	$+2v^2/r$	Centripetal balance; flat rotation curve
1st	$-4v^2 r_s/r^2$	Newtonian gravity: $F = -GMm/r^2$
2nd	$+6v^2 r_s^2/r^3$	GR perihelion precession
3rd	$-8v^2 r_s^3/r^4$	Frame-dragging / Lense–Thirring

Element	Z	Key pair	$\Delta \ln \nu$	$/k_q$
H	1	Ly-α / Balmer limit	1.104	$5.39 \approx 5$
H	1	Balmer / Paschen limit	0.812	$3.96 \approx 4$
He	2	He II / He I 584	0.453	$2.21 \approx 2$
Fe	26	Fe II UV / Fe I optical	0.831	$4.05 \approx 4$
Cs	55	Cs II / Cs I D2	0.616	$3.01 \approx 3$
Rb	37	Rb II / Rb I D2	0.610	$2.97 \approx 3$
Yb	70	$^1P_1$ / repump 1389	1.246	$6.08 \approx 6$

Table 5: Cross-element Karlsson-analogue steps from NIST data [58]. All ratios within $\lesssim 15\%$ of an integer multiple of $k_q = 0.20493$.